Noncovalent functionalization of carbon nanocomposites for electrocatalytic applications

Pedro Diogo Maciel Ferreira
Mestrado em Química
Departamento de Química e Bioquímica
2020

Orientador
Professor Doutor Eduardo Jorge Figueira Marques, Professor Associado, FCUP

Coorientadora
Doutora Diana Mónica de Mesquita Sousa Fernandes, Investigadora Auxiliar, LAQV-REQUIMTE

U.PORTO

FACULDADE DE CIÊNCIAS
UNIVERSIDADE DO PORTO

Todas as correções determinadas pelo júri, e só essas, foram efetuadas.

O Presidente do Júri,

Porto, _____/_____/_____

To my Parents and Grandparents

Acknowledgements

I would like to express my deepest gratitude,

To the Department of Chemistry and Biochemistry of the Faculty of Sciences of the University of Porto, namely its professors and staff, for providing the ideal conditions for a solid formation in Chemistry.

To Professor Eduardo Marques for the opportunity to work in this project, for all the valuable knowledge passed and for the high standards and support demonstrated throughout these years.

To Doctor Diana Fernandes for the scientific and technical orientation, dedication and enthusiasm expressed during the realization of this project.

To Bárbara Abreu for the hours of dedication, support and commitment, without whom this work could not be completed. It was a pleasure working with you.

To all my laboratory colleagues, in particular to Dmitriy Moreira and Rui Machado, for always keeping a good mood and showing companionship.

To all the friends this Faculty has given me, many a few and whose past moments I will take with me forever. Particularly, to Miguel Chaves and Catarina Fernandes: thank you for putting up with me, for the sleepless nights studying, the last-minute reports and late hour laughter sessions that seemed more like therapy.

To the family that the *Residência Universitária do Campo Alegre I* has given me, namely Joana Miranda, Rita Teixeira, Afonso Oliveira, Bruno Cassoni, Francisco Andrade and Flávio Mamede. There is the family where we grow up in, and the family whom we chose to grow up with, and I could not have chosen a better one.

To my girlfriend and best friend, Joana Miranda. It is not an overstatement to say that without you, this would not be possible. Thank you for your support, for always being there for me, even when everything seems lost, and above all, for being who you are.

Em português, porque só assim faz sentido: obrigado aos meus pais, Margarida e Abílio, e aos meus avós, Adelino, Joaquina e Maria, por acreditarem mais em mim que eu próprio. Devo-vos quem sou e o que conquistei, e por muito alto que possa um dia voar, nunca esquecerei as minhas raízes.

Obrigado aos amigos de sempre, de épocas fortes e outras que tais. Acreditem que sem vocês isto não fazia muito sentido. À nossa!

Resumo

Problemas atuais e crescentemente importantes como a poluição decorrente da queima de combustíveis fósseis ou a escassez de combustível têm aumentado a procura de fontes de energia novas e limpas. De entre estas, as pilhas de combustível apresentam-se como fortes candidatas a contribuírem para a resolução do problema, desde que a sua eficiência possa ser aumentada. Neste contexto, os principais objetivos deste trabalho consistem: (i) no desenvolvimento e caracterização de novos materiais nanocompósitos que combinam materiais 1D (nanotubos de carbono, CNTs) e 2D da família dos dicalcogenetos de metais de transição (TMDs) (por ex., MoS_2, $MoSe_2$ e WS_2), utilizando a esfoliação de fase líquida (LPE, *liquid phase exfoliation*) e funcionalização não-covalente assistida por tensioativos; e (ii) em estudos de avaliação de desempenho dos novos materiais como eletrocatalisadores para reações do oxigénio, relevantes paras as pilhas de combustível.

Estudos recentes realizados neste grupo de investigação demonstraram que a quantidade e qualidade do nanomaterial disperso após o processo de LPE assistido por tensioativos podem ser controladas por ajuste de vários parâmetros metodológicos, tais como o tipo e concentração de tensioativo utilizados e os parâmetros associados a processos de ultrassonicação e centrifugação. A funcionalização não-covalente de CNTs e TMDs com tensioativos permite a montagem dos nanocompósitos 3D por um processo coloidal baseado em interações eletrostáticas e o controlo da composição relativa 1D/2D na estrutura final dos nanocompósitos.

Os diferentes materiais de partida e nanocompósitos desenvolvidos foram estruturalmente caracterizados por espetrofotometria de UV-Visível, espetroscopia Raman, medição de potencial zeta e microscopia eletrónica de varrimento (SEM). Posteriormente, os materiais foram avaliados como eletrocatalisadores na reacão de evolução do oxigénio (OER) e na reação de redução do oxigénio (ORR), por voltametria cíclica (CV), voltametria de varrimento linear (LSV) e cronoamperometria (CA). A atividade eletrocatlítica dos novos materiais quanto à ORR é promissora, podendo ser melhorada pelo processo de fabrico implementado. Já a sua atividade eletrocatalítica quanto à OER mostrou-se muito satisfatória. Os resultados mostram ainda que o método utilizado para a construção de novos nanocompósitos é muito versátil, permitindo otimizar o seu desempenho como eletrocatalisadores das reações do oxigénio.

Abstract

Current and increasingly important issues such as the pollution derived from the burning of fossil fuels or the shortage in fuel availability have raised the demand for new, clean and renewable energy sources. Among them, fuel cells have emerged as strong candidates in contributing to solve the problem, provided their efficiency can be increased. In this context, the main objectives of this work are: (i) the development and characterization of new nanocomposite materials combining 1D (carbon nanotubes, CNT) and 2D materials of the transition metal dichalcogenide (TMD) family (e.g. MoS_2, $MoSe_2$ and WS_2), using surfactant-assisted liquid phase exfoliation (SALPE) and non-covalent functionalization; and (ii) the evaluation of the performance of the new materials as electrocatalysts for the oxygen reactions, relevant to fuel cells.

Recent studies carried out in our research group have showed that the quantity and quality of nanomaterial dispersed after the SALPE process can be controlled by adjusting several methodological parameters, such as the type and concentration of surfactant used, and the parameters associated with the ultrasonication and centrifugation processes. The non-covalent functionalization of CNTs and TMDs with surfactants allows both the assembly of 3D nanocomposite materials via a colloidal process based in electrostatic interactions, and the control of the 1D/2D relative composition in the final structure of the nanocomposites.

The different starting materials and nanocomposites developed were structurally characterized by UV-Visible spectrophotometry, Raman spectroscopy, zeta potential measurements and scanning electron microscopy (SEM). Afterwards, they were tested as electrocatalysts in the oxygen evolution reaction (OER) and oxygen reduction reaction (ORR) by cyclic voltammetry (CV), linear sweep voltammetry (LSV), and chronoamperometry (CA). The electrocatalytic activity of the new materials towards ORR is promising and can be improved by the fabrication process developed. Their electrocatalytic activity regarding the OER is very good. The results show also that the method used for the construction of the novel nanocomposites is very versatile, opening the doors for further optimization of their performance as electrocatalysts of the oxygen reactions.

Table of contents

List of figures

List of tables

List of abbreviations, acronyms and symbols

A	Absorbance
c	Concentration of a species
CA	Chronoamperometry
cdc	Critical dispersibility concentration
cmc	Critical micelle concentration
CNFs	Carbon nanofibers
CNTs	Carbon nanotubes
C_{O2}	Bulk concentration of O_2
CPyCl	Cetylpyridinium chloride
CQDs	Carbon quantum dots
c_{surf}	Concentration of surfactant
CTAB	Cetyltrimethylammonium bromide
c_{TMD}	Concentration of TMD
CV	Cyclic voltammetry
CVD	Chemical vapor deposition
D_{O2}	Diffusion coefficient of O_2
DTAB	Dodecyltrimethylammonium bromide
DWNT	Double-walled carbon nanotube
E	Electric potential
$E°$	Standard electric potential
$E°_{Ag/AgCl}$	Standard electric potential *vs.* Ag/AgCl
$E_{Ag/AgCl}$	Electric potential *vs.* Ag/AgCl
E_{onset}	Onset potential
E_{pc}	Potential of the cathodic peak
E_{RHE}	Electric potential *vs.* RHE

F	Faraday's constant
$f(\kappa\alpha)$	Henry function
H	Hexagonal coordination
HER	Hydrogen evolution reaction
HOR	Hydrogen oxidation reaction
IGAs	Inorganic graphene analogues
j	Current density
j_0	Exchange current density
$j_{1.8}$	Current density at E = 1.8 V *vs.* RHE
j_k	Kinetic current density
j_L	Diffusion-limited current density
j_{max}	Maximum current density
l	Path length
L_m	Median MLD
LSV	Linear sweep voltammetry
M	Metal (in TMD)
MLD	Mean lateral dimension
MWNTs	Multi-walled carbon nanotubes
n_{O2}	Number of electrons transferred per O_2 molecule
N-MWNTs	Nitrogen-doped multi-walled carbon nanotubes
OER	Oxygen evolution reaction
ORR	Oxygen reduction reaction
POMs	Polyoxometalates
RDE	Rotating disk electrode
RHE	Reversible hydrogen electrode
R_u	Circuit uncompensated resistance
SALPE	Surfactant assisted liquid phase exfoliation

SC	Sodium cholate
SDBS	Sodium dodecylbenzenesulfonate
SDS	Sodium dodecyl sulfate
SEM	Scanning electron microscopy
STS	Sodium tetradecyl sulfate
SWNT	Single-walled carbon nanotube
T	Trigonal prismatic coordination
T_{Kr}	Krafft Temperature
TMDs	Transition metal dichalcogenides
TS	Tafel slope
TTAB	Tetradecyltrimethylammonium bromide
U_E	Electrophoretic mobility
UV-Vis	Ultraviolet-visible spectrophotometry
v	Scan rate
w	Width of log-normal curve
X	Chalcogen (in TMD)
ε	Extinction coefficient
ε_r	Dielectric constant
ζ	Zeta potential
η	Overpotential
μ	Medium viscosity
v	Kinematic viscosity
σ	Standard deviation
ω	Angular velocity

Chapter 1

Introduction

1 Introduction

1.1 Aims and Scope

This interdisciplinary work combines theoretical and practical aspects of different and trending fields of Chemistry: Surface and Colloid Chemistry, Materials Chemistry and Electrochemistry. The main goal is to assemble, in a facile and versatile method, nanocomposite materials that can be explored and applied as electrocatalysts in regards to both the Oxygen Evolution Reaction (OER) and the Oxygen Reduction Reaction (ORR). To achieve this, two more specific goals were defined. Using concepts and methods from the two first fields, namely surfactant-assisted liquid phase exfoliation, the initials goals of this work are to assemble, in a controlled and replicable manner, nanocomposite materials of carbon nanotubes and graphene-like materials, and to characterize them structurally. The next goal is to apply the novel materials in OER and ORR electrocatalytic studies, assessing their viability as proof-of concept functional materials. By adjusting several methodological parameters of the assembling process, the final characteristics of the materials can be changed, which, in turn, affects the materials' electrocatalytic capabilities.

It is, therefore, an innovative work in the sense that it brings together different fields of study, tackling a problem that has global consequences: the sluggish kinetics of the OER and ORR reactions and the expensive noble metal-based electrocatalysts that make the implementation of fuel cells non-competitive. To better understand this issue, we begin this introduction by assessing the world energy problem, what it is and what is being done to address it. What follows is a focus on the fuel cells, its working principle and kinetic issues, showing various novel materials that try to address this problem. The third part of this introduction will delve with carbon nanomaterials, graphene-like materials, and composite nanomaterials, for a thorough understanding of the materials dealt with in this work. To understand how the nanocomposite materials are assembled, the fourth and last part will look at some of the most common preparation methods, with emphasis in the surfactant-assisted liquid phase exfoliation.

1.2 The world energy problem

In 1799, Alessandro Volta developed the first ever battery.[1] This discovery opened society to the wonders of electricity while, at the same time, laid the foundations for a problem that would take years to unfold: society's dependence on energy and the ensuing environmental problems. If, on the one hand, technological advances demand ever higher energy production, on the other hand, today, this production relies mostly on fossil sources. Fossil fuels are finite, with projections going as far as saying that by 2040 all oil reserves will be extinct,[2] which in itself is a problem that needs remedy. But fossil fuels are also very pollutant, since they need burning which releases harmful gases to the environment.

Renewable energy sources solve a great deal of the environmental problems, but cannot, alone, tackle the growing energy demand problem, since these rely on sources that are not always available and have low efficiency rates.[3] As such, the search for energy solutions should take into account the development of new technologies that allow energy conservation and storage, mitigating the effects of the growing energy demand.[4]

Long-lasting and clean energies are vital to the development of future energetic sustainability. The search for electrocatalysis-mediated energy conversion processes has delivered some technologies that, when coupled with renewable energies, are capable of converting molecules present in the atmosphere (water, nitrogen or carbon dioxide) in added-value products (hydrogen, hydrocarbons and ammonia). Such processes can be found in many energy storage and conversion devices like metal-air batteries and fuel cells.[5, 6]

1.3 Fuel cells

Fuel cells are electrochemical devices, resembling a battery, that convert the chemical energy present in the fuel molecules directly into electric energy. In general, they have high conversion efficiencies and are not limited by thermodynamic limitations, since the intermediate steps of heat and mechanical work are avoided. In addition, they are environmentally safe since there is no combustion. Contrary to what happens in a battery, the chemical compounds necessary to generate energy are sourced from outside the cell.[7]

1.3.1 Working principle

Figure 1 represents, as an example, a schematic illustration of a hydrogen fuel cell and an electrolytic cell. These systems are based on the hydrogen cycle (or water cycle) and, in general terms, work as follows:

- **Electrolytic cell.** It uses electricity (from renewable sources, for example) to split the water into H_2 (fuel) and O_2 as shown in equation (1). At the cathode, the Hydrogen Evolution Reaction (HER) takes place, while at the anode the Oxygen Evolution Reaction (OER) occurs.[8] This powerful energy conversion method also serves as an alternative to the steam reforming of fossil fuels to produce H_2,[8] that releases harmful gases to the environment and should be avoided.[9]

$$2H_2O\ (l) \rightarrow 2H_2\ (g) + O_2\ (g) \qquad (1)$$

- **Hydrogen fuel cell.** The fuel (i.e. previously produced H_2) reacts with O_2 to produce electric energy and water as the major product. At the cathode, there is reduction of O_2 (ORR) while at the anode H_2 is oxidized (Hydrogen Oxidation Reaction, HOR).[8]

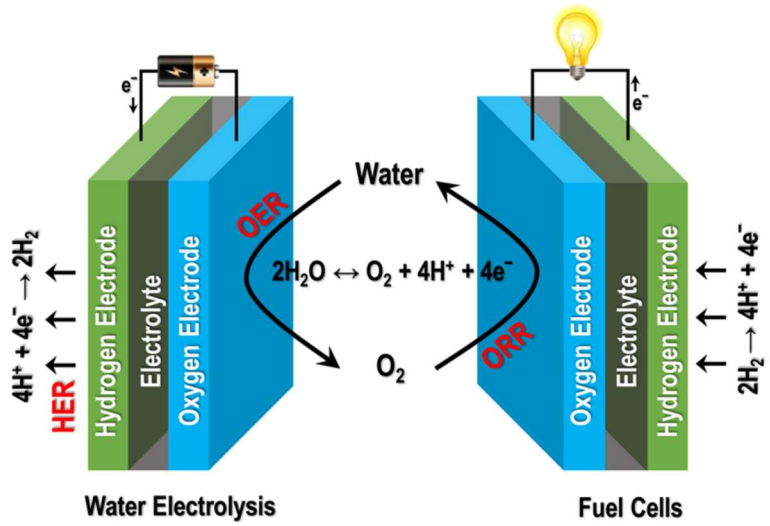

Figure 1 – Schematic representation of a hydrogen fuel cell and electrolytic cell and their principle of operation. Reproduced from ref. [10]

The life cycle and efficiency of fuel cells is largely favored by high purity H_2. Since the electrolytic cell allows the production of high purity H_2 (without CO_2), these work best combined, closing the energy conversion cycle without carbon emissions.[8, 11]

Charge and discharge processes of these devices are dominated by the oxygen-based reactions, OER and ORR, respectively. However, the kinetics of these reactions are slow, making them difficult to trigger. As such, electrocatalysis plays a fundamental role on the implementation of these clean energy production technologies: the electrocatalytic process is vital in increasing the rate, efficiency and selectivity of the chemical reactions.[5, 8, 12]

1.3.2 The oxygen reactions

Oxygen reactions relates to the OER and ORR, involving oxygen molecules being generated or reduced, respectively. In general terms, OER is the generation of O_2 from the electrochemical oxidation of water. This can be achieved via two ways: in neutral or acidic electrolytes, two molecules of H_2O are oxidized into four protons and one O_2 molecule, as shown in equation (2); in alkaline electrolytes; four hydroxide ions are oxidized into two water molecules and an O_2 molecule, as shown in equation (3).[8]

$$2H_2O\ (l) \rightarrow 4H^+ + O_2\ (g) + 4e^- \quad (2)$$

$$4OH^- \rightarrow 2H_2O\ (l) + O_2\ (g) + 4e^- \quad (3)$$

As for the ORR, in aqueous electrolytes, O_2 gas molecules can be reduced in two alternative manners. Table 1 summarizes the two possible pathways, as well as showing the standard electrode potentials ($E°$) for each reaction. In short, this reaction can occur via a direct four electron ($4e^-$) pathway in which O_2 gets four electrons, generating water in acidic electrolytes or hydroxyl groups in alkaline electrolytes. Alternatively, it can occur through an indirect two steps of two electrons each ($2e^-$), in which O_2 gains two electrons and H_2O_2 (in acidic electrolytes) or HO_2^- (in alkaline electrolytes) are generated as intermediates, and then are further reduce to water.[8, 13]

Table 1 – Reaction pathways of ORR in aqueous solution[8]

Electrolyte	Reaction pathway
Acidic	4-electron $O_2 + 4e^- + 4H^+ \rightarrow 2H_2O$ ($E°$ = 1.229 V) 2-electron $O_2 + 2e^- + 2H^+ \rightarrow H_2O_2$ ($E°$ = 0.695 V) $H_2O_2 + 2e^- + 2H^+ \rightarrow 2H_2O$ ($E°$ = 1.763 V)
Alkaline	4-electron $O_2 + 4e^- + 2H_2O \rightarrow 4OH^-$ ($E°$ = 0.401 V) 2-electron $O_2 + 2e^- + H_2O \rightarrow HO_2^- + OH^-$ ($E°$ = -0.065 V) $HO_2^- + H_2O + 2e^- \rightarrow 3OH^-$ ($E°$ = 0.867 V)

1.3.2.1 Kinetics

The general mechanisms shown do not fully address the complexity of the OER and ORR mechanisms. It is a multistep process involving multiple adsorbed intermediates, which primarily depend on the properties of the electrode surface.[14] Some of the important steps involve the initial O_2 adsorption, followed by the oxygen-oxygen bond breaking and subsequentially the formation of oxygen adsorbed species.[14, 15]

Particularly, the high energy of the oxygen-oxygen bond (498 kJ·mol^{-1}) that has to be broken, makes the kinetics of these reactions very sluggish and not easily activated electrochemically. In order to do so, one must apply high reduction potentials, which decreases the lifetime and performance of fuel cells. It is, therefore, crucial to use some type of electrocatalyst.[13]

1.3.2.2 Benchmarking electrocatalysts

Several kinetic parameters are commonly used to evaluate the performance of a certain electrocatalyst. For the OER, these parameters include:

- The **overpotential (*η*)**, defined as the difference between the applied potential and the equilibrium, or thermodynamically determined reduction potential. It is related to the current density, *j*, when solely limited by the electrode reaction's kinetics. Usually, it is also referred as j = 10 mA·cm^{-2}, or the potential at which this value of current

density is attained. This *j* value is expected for a 12.3 % efficiency in solar to hydrogen devices, a requirement for cost-competitive photoelectrochemical water splitting.[8, 16]

- The **exchange current density (j_0)**, the exchange current normalized to unit area. Exchange current relates to the intrinsic electrocatalytic activity of the electrocatalysts, in equilibrium conditions.[8, 16]
- The **Tafel slope (TS)**, related to the electrocatalytic mechanism of the electrode reaction and that can be obtained by fitting the linear part of the Tafel plot (η *vs.* logarithm of j).[8]

A good OER electrocatalyst should present low values of η and TS, while presenting high values of j_0. Currently, RuO_2 and IrO_2 are considered the benchmark OER electrocatalysts, showing the highest activity.[14]

To evaluate the ORR performance of electrocatalysts, the parameters used are:[8]

- The **onset potential (E_{onset})**, defined as the potential at which the reaction starts. It can be calculated via two distinct methods: 1) the potential at 5% of the maximum current (j_{max}), or 2) the potential at a current (j) of 0.1 $mA \cdot cm^{-2}$.
- The **diffusion-limited current density (j_L)**, a current density reached when the reaction at the electrode is only controlled by mass transportation (the rate of diffusion of the reactant to the electrode becomes independent of the applied potential, a plateau is reached and $j = j_L$).
- The **kinetic current density (j_k)**, the measured current density when there are no mass-transfer limitations.
- The **number of electrons transferred per O_2 molecule (n_{O_2})**, which provides the selectivity of the electrocatalyst towards the 2- or 4-electron pathway.
- The **Tafel slope (TS)**, as already explained.

A good ORR catalyst should offer lesser negative E_{onset} values, high values of j_L, low TS values and, preferably, a selectivity towards the 4-electron pathway, since the production of the hydrogen peroxide intermediate can lead to the corrosion of the device's components.[8] Nonetheless, electrocatalysts selective for the 2-electron process are useful in industrial H_2O_2 production. It is worth mentioning that, when dealing with a 2-electron selective electrocatalyst, lower j_L does not necessarily mean a less active catalyst, as this parameter takes into account the pathway selectivity.[17] Currently, platinum nanoparticles supported on carbon materials (Pt/C) are the most effective ORR electrocatalyst.[12]

1.3.3 Novel electrocatalysts for the oxygen reactions

Apart from a good performance in the aforementioned kinetic parameters, electrocatalysts should also exhibit high stability/durability and resistance to fuel (e.g. methanol) crossover, something that the noble metal electrocatalysts used today do not possess. That, allied with their scarcity and high price, makes current electrocatalysts economically unviable, spurring the search for alternatives that are more stable and cost-effective.[8, 12, 14] In addition, electrocatalysts should preferably be bifunctional to the two oxygen reactions. However, although platinum based electrocatalysts are the best for ORR, they are not effective for OER (Pt oxidizes easily at large overpotentials). Likewise, good OER catalysts are less effective for ORR.[6]

Carbon materials have emerged as potential alternatives to platinum-based electrocatalysts, and, therefore, have been extensively studied. Graphite[18], N-doped carbon nanotubes[19, 20], N-doped graphene[21] and carbon quantum-dots (CQDs)[22, 23] have been reported to have good electrocatalytic behavior towards ORR. Graphene quantum dots, either heteroatom-doped[24] or decorated with non-platinum metals[25, 26], have also been described as good ORR catalysts. Hybrids of N-doped CNTs with N-doped graphene[27] or graphene oxide/Fe have been reported on their bifunctionality for both oxygen reactions.

Many other materials have been shown to have good electrocatalytic behavior toward the oxygen reactions, such as polyoxometalates (POMs),[12] perovskites,[28] organometallics[29] or spinel family[30] compounds. Transition metal dichalcogenides (TMDs) have been extensively reported on their good HER catalyst activity.[31-33] However, their use for the oxygen reactions has been scarcely addressed before and this is one main driving force for the current work.

1.4 Carbon nanomaterials

Carbon has some special valency properties and is, therefore, capable of forming many allotropes, with a huge variety of characteristics, spanning from one extreme to the other. Consider diamond and graphite, for instance: diamond is transparent and the hardest known material, while graphite is black opaque and soft; diamond is an electrical insulator, while graphite has high electrical conductivity.[34]

Thirty years ago, with the discovery of C_{60} fullerenes[35] and carbon nanotubes (CNTs)[36], carbon nanomaterials started to gain some attention in the scientific

community, due to their high chemical and thermal stabilities, good electrical properties, high mechanical strength, surface area and porosity.[37] Graphite, diamond, fullerenes, CNTs and graphene are among the most studied and reported allotropic forms of carbon.

1.4.1 Graphene

Graphene is the basic structure of all sp^2 hybridized carbon allotropes. It is a tightly packed single layer of carbon atoms (2D material, since only one dimension is restricted), bonded in an hexagonal honeycomb-like lattice, as shown in Figure 2.[38] Two very important characteristics of graphene are its high surface area (2630 $m^2 \cdot g^{-1}$)[39] and the fact that all the edges of the sheet are available for molecular absorption phenomena. The large delocalized π-electron system can form strong π-stacking interactions. When several layers of graphene are stacked on top of each other in well-organized crystalline structure, graphite is formed.[38]

Recent studies[40-42] have tried to tackle the problem of a lack of industrial means of producing graphene. Once this is obtained, graphene will finally be a real contender to be used in widespread technologies.[43]

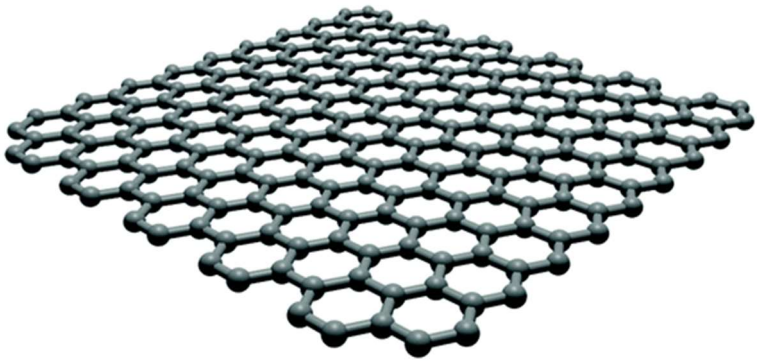

Figure 2 – Molecular structure of graphene. From ref.[44]

1.4.2 Carbon nanotubes (CNTs)

Carbon nanotubes consist of graphene layers rolled into cylinders. Depending if they involve a single graphene sheet, or several concentric sheets, CNTs are classified as single-walled (SWNTs) or multi-walled (MWNTs), respectively (Figure 3). These structures have few nanometers in diameter, but can have lengths in the order of

micrometers.[45] Their surface area can vary between 150 (MWNTs) and 1500 $m^2 \cdot g^{-1}$ (SWNTs).[46, 47]

CNTs are generally produced by four main methods: arc discharge, laser ablation, molten salt intercalation, and chemical vapor deposition.[48] Chemical vapor deposition is the most popular method of producing CNTs, since it offers more control over the length and structure of CNTs, when compared to arc discharge and laser ablation methods.[49] Generally, the procedure starts by introducing a mixture of hydrocarbons, metal catalysts and an inert gas into a reaction chamber. Then, at temperatures of 1000-12000 K and at atmospheric pressure, the hydrocarbons start decomposing and CNTs form on the substrate. The diameters of the final product are related to the size of the metal particles.[49]

CNTs offer unique electric, thermal and mechanical properties combined in a single material, making them ideal for functionalization and later application in a wide variety of technologies.[50] An adequate modification to CNTs can potentiate new and improved characteristics, making these one of the most used nanomaterials to serve as the basis of novel structures.

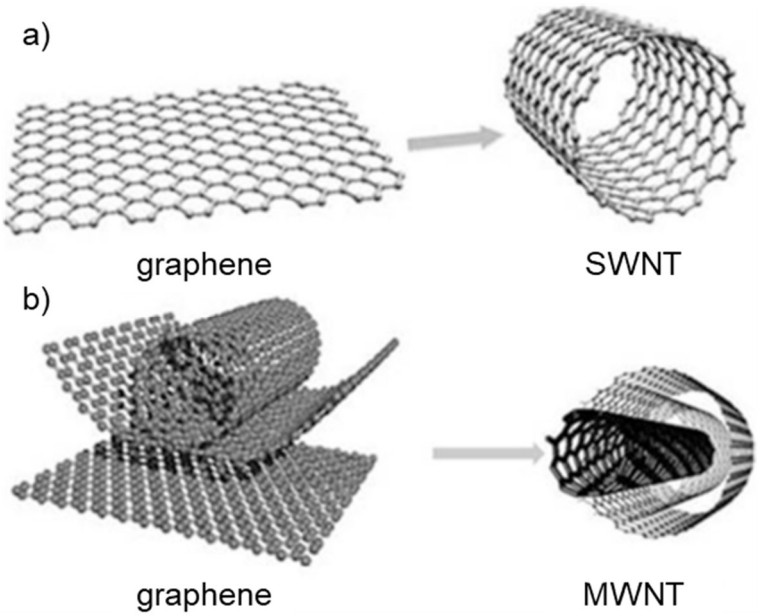

Figure 3 – Molecular structures of a) single walled carbon nanotubes (SWNT) and b) multi walled carbon nanotube (MWNT). Adapted from ref.[51]

1.4.3 Doped carbon nanomaterials

As stated above, fine tuning of the physicochemical properties of CNTs by chemical modification is necessary in many applications.[52] One means of achieving this is by elemental doping, whereby small concentrations of different molecules or compounds (from parts per million to small weight percentages) are introduced into the matrix of the nanomaterials.[53] This is attained by three different manners (Figure 4): **filling**, or **endohedral doping**, where doping agents are introduced inside CNTs; **intercalation**, or **exohedral doping**, where doping agents are introduced in the interstices of the CNTs; **substitution**, or **in-plane doping**, where doping agents are introduced in the matrix of C atoms of the CNTs, substituting some of them.[54]

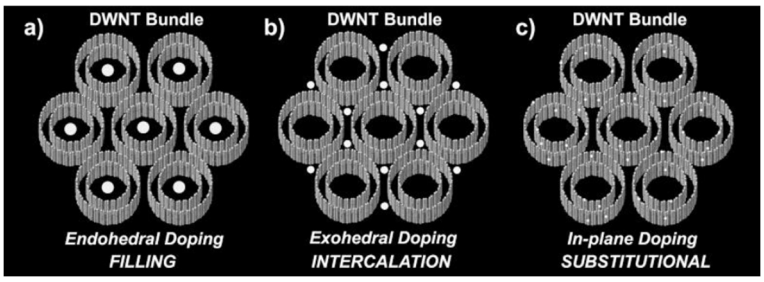

Figure 4 - Molecular models representing schematically (a) filling, (b) intercalation and (c) substitutional doping in double-walled carbon nanotubes (DWNT) bundles. From ref.[54]

More specifically, substitutional doping relates to the removal of one or several C atoms from the crystalline structure of a pristine CNT, and their substitution with heteroatoms such as nitrogen (N). This results in CNTs that have a different wall configuration, making the rugosity and defects of the outer walls particularly appealing, as it improves the tube covalent chemistry. The resulted high wall reactivity of N-doped CNTs makes them ideal components as matrix fillers in composite materials.[55]

There are several processes to produce N-doped CNTs:[54, 56]

- **Arc discharge –** arcing doped graphite or graphite electrodes in an inert atmosphere;
- **Laser ablation –** vaporizing carbon from a graphite target at high temperature, using a high power laser;

- **Chemical Vapor Deposition (CVD) –** thermally decomposing N containing hydrocarbons over metal particles (e.g. Fe , Co, Ni);
- **B and N substitution reactions –** using potential substitution in the presence of B_2O_3 vapor and N_2 at 1500-1700 K.
- **Plasma assisted CVD –** same CVD method, but producing large areas of aligned N-doped MWNTs.
- **Mechanochemical treatment** – ball milling with appropriate precursors followed by a thermal treatment in an inert atmosphere.

1.4.4 Graphene-like materials

Graphene-like materials are those which comprise a single layer or few layers composed of atoms other than carbon, in a structure analogous to that of graphene.[57] The methodology applied in the discovery of graphene was extended to other materials[58] and single layers from a variety of layered materials (such as *hexagonal*-BN, MoS_2, $NbSe_2$ and $Ba_2Sr_2CaCu_2O_x$) were isolated.[59]

As with all nanomaterials, inorganic graphene-analogues (IGAs) can be obtained by two approaches, bottom-up and top-down, both of which have advantages and limitations.[58] As a bottom-up approach, CVD can be successfully applied, with the advantage being the control over the thickness and growth of the 2D particles. A metal substrate serves not only as surface and template on which the particles grow, but also as a catalyst to assist the process. Surface-assisted epitaxial growth, deemed as a modification of the CVD method, can also be applied. In this method, the metal substrate serves as a seed crystal, rather than a template or catalyst.[57]

Top-down approaches, generally, have the benefit of being easy and fast ways of obtaining highly crystalline nanosheets. Micromechanical cleavage is the original method used in the peeling off of graphene from graphite: layers are peeled from layered materials such as graphite or *h*-BN. The most used method, however, is chemical exfoliation, as it can equally isolate single and few layer particles, but in larger quantities. It consists of applying mechanical energy (for instance, by the processes of ultrasonication, ball milling or sheer mixing) to the layered bulk material to peel off the layers.[57]

An important class of 2D graphene analogues are the transition metal dichalcogenides.

1.4.4.1 Transition metal dichalcogenides (TMDs)

Transition metal dichalcogenides are compounds formed by two chalcogenide atoms (namely sulfur, selenium and tellurium) covalently bonded with a transition metal, with general formula MX_2, M being the metal and X being the chalcogenide. As with graphene, these materials are layered, *i.e.*, composed of 2D sheets stacked on top of each other. In each sheet, the metal center has either a trigonal prismatic (H = hexagonal) or octahedral (T = trigonal prismatic) environment.[60] As an example, MoS_2, one of the most studied TMDs, has a trigonal prismatic (when viewed from the top, it forms a hexagonal, or honeycomb, lattice) configuration, with layers 6.5 Å apart (Figure 5).

These sheets have the thickness of three atoms, with the metal atom sandwiched between the two chalcogen atoms. Layers are held together by weak interlayer forces (van der Waals interactions).[60] The weak forces between layers make these materials ideal for application as solid lubricants.[61] Other applications include the use of these materials, namely MoS_2, in electronic applications, as bio or gas sensors and supercapacitors.[62]

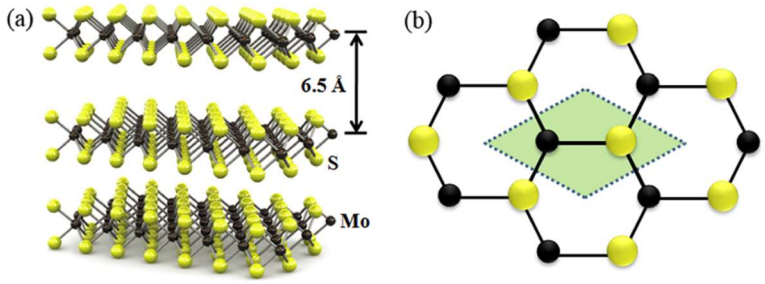

Figure 5 – Molecular structure of MoS_2, a TMD: a) side view of the three atoms thick layers, with S-Mo-S configuration; b) top view of the hexagonal lattice formed by Mo and S atoms. From ref.[63]

1.4.5 Nanocomposites

Composites are materials that contain at least two components with distinct physical and chemical properties. Typically, one phase (filler) is dispersed in a second one (matrix). The filler is used to enhance the overall properties of the matrix, by usually adding mechanical, thermal or electrical abilities.[48, 64] When mixed, the different constituents of the composite form a material with enhanced or unique assets.

Synergism is attained when the benefits of the composite are higher than the sum of the benefits of each individual constituent.[65]

Nanocomposites share most of the definition with conventional composites, except that these materials have one or more constituents with at least one dimension in the order of nanometers.[66] The reduction from micro-range to nano-range of the constituents provides remarkable reinforcement to the material. For example, replacing traditional composites such as carbon fiber or glass fiber with CNTs or carbon nanofibers (CNFs) nanocomposites gives the final material higher strength-to-weight ratio and flexibility.[67]

Carbon nanomaterials have been thoroughly implemented in nanocomposites, due to their superior properties.[68] These, in turn, have been successfully applied, in very distinct fields, as electromagnetic interference shields,[69] supercapacitors,[70] gas sensors,[71] or biosensors.[72] Particularly in the field of electrochemistry, carbon based nanocomposites have become very attractive materials for energy storage solutions. This is especially true for 1D carbon structures (CNTs, CNFs, etc.). Owing to their anisotropic properties, that provide fast electron axial transport with short pathways for ion diffusion and large specific surface areas,[73] CNT and CNF based nanocomposites have been applied as the anode in sodium-ion batteries.[74-76]

Recently, TMD/carbon nanocomposites have emerged as good contenders for energy storage and conversion applications.[77] MoS_2 has been used in combination with graphene[78, 79] and CNT[80, 81] to assemble nanocomposites as electrocatalysts for HER. These materials are typically synthesized through hydrothermal/solvothermal reactions, involving high-temperature conditions and toxic reducing agents.

1.5 Preparation and assembly of functional nanomaterials

The functionalization of materials, particularly, carbon nanomaterials such as graphene or CNTs consists of, mainly, the modification of the surface of these materials with any compound. As a result, this process alters the inherent properties of the material, which can be used to tailor its physicochemical properties.[82] With regard to graphene and CNTs, functionalization is of vital importance for their applications, since functionalization can enhance dispersibility and prevent the agglomeration.[83, 84] This can be achieved covalently or noncovalently, using several different methods.

1.5.1 Covalent functionalization

Covalent functionalization of carbon nanomaterials involves covalently attaching a variety of functional groups, either on the edge or on the surface of graphene or CNTs. It involves the rehybridization of one or several sp^2 C atoms of the lattice into the sp^3 configuration. This makes it possible for a functional group to be bonded, altering solubility or producing a material that is suitable for some application.[83, 84]

Regarding graphene, covalent functionalization can be achieved in four different ways: nucleophilic substitution, electrophilic addition, condensation, and addition reactions.[84] As for CNTs, sidewall functionalization involves cycloaddition and radical addition reactions, while end-tip functionalization is achieved by oxidation, esterification and amidation reactions.[83]

1.5.2 Noncovalent functionalization

Noncovalent functionalization is of particular interest since it allows the decoration of carbon materials surface without disturbing the characteristic delocalized π-electron system.[83] These interactions involve hydrophobic, van der Waals, and electrostatic forces, and are achieved by the physical adsorption of suitable molecules on the surface, such as surfactants, small aromatic molecules, porphyrins, peptides and even biomolecules such as DNA.[84]

Usually, this process starts with the exfoliation of graphene layers or the debundling of CNT agglomerates. This is achieved by ultrasonicating a dispersion of the carbon nanomaterial in a liquid. Ultrasounds create mechanical waves in the fluid, which, in turn, create high- and low-pressure zones. This difference in pressure promotes high speed fluid movement, capable of overcoming the van der Waals cohesive forces,[85] resulting in the exfoliation of the graphene layer/CNT from the bulk reservoir. The functionalization molecules in solution adsorb in the recently exposed surface, isolating the particle and promoting stability. Otherwise, the exfoliated nanomaterials would rapidly aggregate and revert to their original agglomerated state.

1.5.2.1 Surfactants

Surfactants are amphiphilic molecules — the same molecule has a hydrophilic polar “head” and an hydrophobic nonpolar “tail”. This characteristic means that surfactants can

adsorb on the interface of any polar-nonpolar system, reducing the interfacial tension.[86] Another fundamental property of surfactants is that unimers (unassociated surfactant molecules) tend to form aggregates, called micelles, when in solution. This process is called self-assembly and depends on the concentration of surfactants in the solution, with the concentration at which micelles start to form designated as critical micelle concentration (*cmc*).[86, 87]

Both the adsorption and self-assembly properties make surfactants ideal candidates to be used as functionalizing agents, since they can easily adsorb to any surface, and, when above the *cmc*, micelles can be seen as a reservoir of unimers.[87] This is especially interesting in the case of CNTs, graphene or TMDs. Since they all are hydrophobic materials, the nonpolar "tails" of surfactants can easily adsorb to their surface, while polar "heads" make the overall functionalized material water-soluble. As such, surfactants have been successfully used in the noncovalent functionalization of graphene[88, 89] and CNTs,[90-92] in a process called surfactant-assisted liquid phase exfoliation (SALPE).

When ultrasonicated in an aqueous solution of a given surfactant, the shearing forces caused by the ultrasounds will peel the layers of a 2D material, or isolate CNTs that were agglomerated. Surfactants will, then, adsorb to the surface of these materials, exposing their polar heads, which enhances the dispersibility of these materials in polar solvents, and prevents restacking or regrouping (Figure 6). By adjusting the methodological parameters of this process, the concentration and characteristics of the dispersed material can be changed, as reported previously by our research group.[90-92]

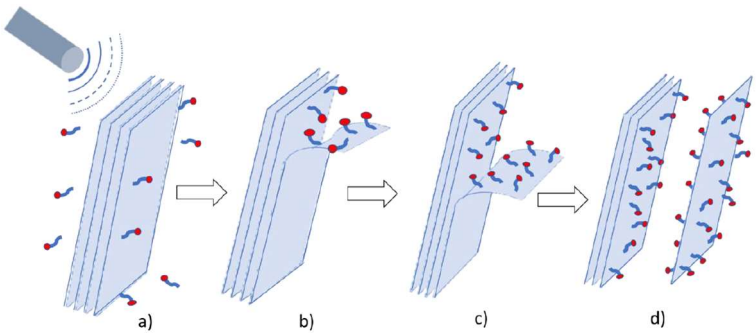

Figure 6 – Schematic representation of the surfactant assisted liquid phase exfoliation process on a 2D material: a) bulk material is exposed to ultrasonication; b) shearing forces start pealing the external layers; c) surfactants start adsorbing on the newly exposed surfaces; d) a single-layer of the material is pealed from the bulk, and the surfactants adsorbed to its surface avoid regrouping.

Particularly, Fernandes *et al.*[92] resorted to carefully controlled experimental procedures and statistical sampling to extract some metrics that evaluate the performance of a surfactant when dispersing CNTs. These include, among others, the critical dispersibility concentration (*cdc*), which is the minimum surfactant concentration required to effectively start dispersing the CNTs; the maximum concentration of CNT attainable with a certain surfactant, $c_{CNT,max}$; and the concentration of surfactant at which point $c_{CNT,max}$ is attained, $c_{surf,max}$. Furthermore, high precision dispersibility curves for CNTs in different surfactant aqueous solutions were presented (Figure 7), setting the base for the dispersibility studies of 2D materials presented in this work.

Generally, the curves have a sigmoidal profile, with c_{CNT} rising steeply beyond the *cdc*, then tends to a plateau value, after which it drops dramatically. Further, results show that anionic surfactants are slightly better dispersants than cationic, and that, ultimately, it is surfactant availability and binding affinity to the CNT surface that dictate the effectiveness and efficiency of the process.

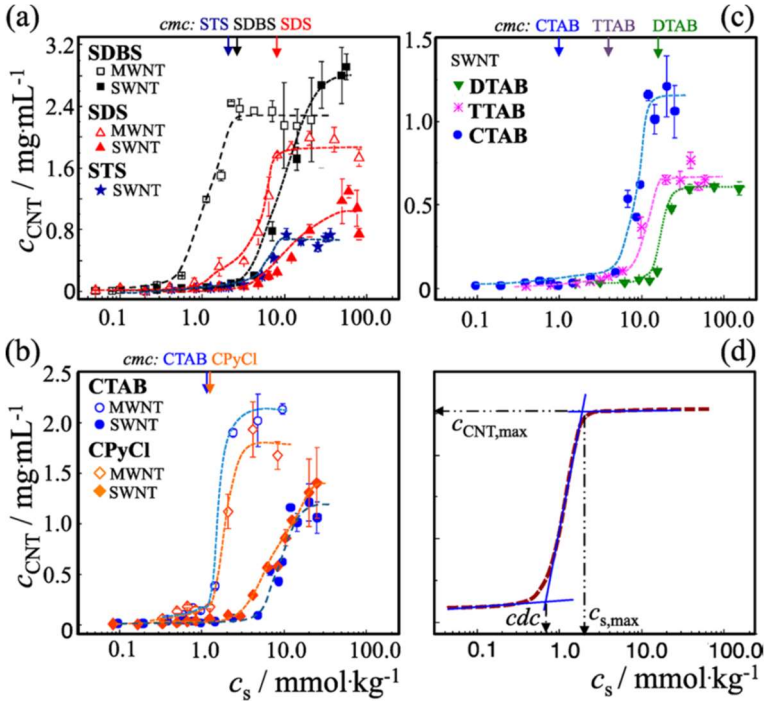

Figure 7 – Dispersibility curves of MWNTs and SWNTs in different surfactants (logarithmic scale). (a) anionic surfactants SDBS, SDS and STS; (b) cationic surfactants CTAB and CPyCl; (c) homologous series DTAB, TTAB, and CTAB; (d)representative curve with the graphical definition of the dispersion parameters. From ref.[92]

Despite several studies and the reported effectiveness of this process, the mechanisms of dispersion and microscopic configurations of the surfactants around CNTs and other carbon nanomaterials is still being unraveled, at molecular level.[90, 91] Regardless, in practice, non-covalent functionalization of carbon surfaces can be attained in a facile manner by the adsorption of amphiphiles, like surfactants and surface-active polymers, on the hard nanomaterial surface, thus changing some of its interfacial properties like hydrophilicity, wettability and surface charge. The colloidal kinetic stability of the dispersed nanomaterial is also increased due to steric or electrostatic repulsions between the amphiphile-coated surfaces. Since no chemical reactions occur, and the process is usually performed in mild conditions (i.e. aqueous media, low temperature) non-covalent functionalization constitutes indeed a path to tune the physical properties of 1D and 2D nanomaterials without compromising the material´s intrinsic properties.

Chapter 2

Experimental Section

2 Experimental section

Reactants, materials and solvents, assembly methods of the nanocomposites, as well as instruments, techniques and procedures of the characterization methods are described in this chapter.

2.1 Materials

The TMDs used in the dispersibility studies and assembly of the nanocomposites were MoS_2 (Sigma-Aldrich, >99%) and WS_2 (Sigma-Aldrich, >99%). $MoSe_2$ (Sigma-Aldrich, >99%) was also used in dispersibility studies. The MWNTs (diameter of 8-15 nm) used to assemble the nanocomposites were purchased from Cheaptubes®. The surfactants used in both the dispersibility studies of TMDs and assembly of nanocomposites were cetyltrimethylammonium bromide (CTAB, Sigma-Aldrich, >99%) and sodium cholate (SC, Sigma-Aldrich, >99%). Tetradecyltrimethylammonium bromide (TTAB, Sigma-Aldrich, >99%) was used to disperse MWNTs when assembling the nanocomposites.

In the initial plan of this work, N-doped CNTs and graphene were to be synthesized via ball milling method followed by thermal treatment and their performance as electrocatalysts was to be studied. However, due to time constraints, previously synthesized N-doped multiwalled carbon nanotubes (N-MWNTs) were used to assemble the final nanocomposite materials. N-MWNTs were kindly supplied by Doctor Bruno Jarrais, and were synthesized by a mechanochemical treatment (ball milling) followed by thermal treatment at 600º C in an inert atmosphere, as shown in ref.[93] This method used melamine as the N source.

In the electrochemical studies, isopropyl alcohol (Sigma-Aldrich, >99,5%) and Nafion 117 (Aldrich, 5 wt% in a water and aliphatic alcohols solution) were employed in the preparation of the dispersions used to modify the electrodes. Potassium hydroxide (KOH, Sigma-Aldrich, >99.99%) was used as electrolyte.

Ultrapure water (Millipore™), with electrical resistivity of 18.2 MΩ·cm at 25 °C, was used throughout every step of the assembly and characterization processes.

2.2 Preparation methods

2.2.1 Dispersibility studies – sample preparation and quantification of dispersed materials

To study the dispersibility behavior of the TMDs in surfactant solutions, mixtures containing the same quantity of TMDs and different concentrations of surfactant were prepared. The process (based on previous reports[92]) began with weighing 60 mg of TMD, followed by the addition of 20 mL of aqueous surfactant solution (variable concentration), which results in a 3 $mg \cdot mL^{-1}$ loading. The aqueous surfactant solutions were pre-prepared using ultrapure water, and kept at temperatures above the Krafft temperature (T_{Kr}) of the surfactant to ensure full dissolution.

These mixtures were then ultrasonicated using a Sonics VC 505 probe (500 W output power; 20 kHz processing frequency) with a freshly polished 13 mm tip, placed 1 cm above the bottom of the plastic flask. Vibration amplitude was set to 50% and sonication was maintained for 23 min. An external bath set to 10 °C and magnetic agitation was used to avoid overheating. After sonication, the samples were centrifuged using a Centurion Scientific K241R centrifuge. TMD dispersions were centrifuged for 10 min at 1500 g, and the supernatant was recovered to a new flask for posterior analysis.

Quantification of dispersed nanomaterial. To determine the concentration of TMDs dispersed, c_{TMD}, a spectroscopic method was employed, which allowed the determination of the extinction coefficient, ε. A sample was ultrasonicated and centrifuged in neat H_2O (no surfactant involved in the process), and the supernatant was recovered. Part of it (1 mL) was used to measure the apparent absorbance, A. The rest was put in an oven (40 °C) until all the water was evaporated. The mass difference was registered, and with it, c_{TMD} in neat H_2O was determined.

From this value, the ε was determined by successively diluting the neat H_2O dispersion. The apparent absorbance was measured for each dilution and plotted against the c_{TMD}. An example of these plots is presented in Figure 8 (A *vs.* c_{MoSe2}). Similar ones were built for other TMDs. Since the results present a linear fit, Lambert-Beer's law (equation (4)) was applied and the extinction coefficient was determined.

This process was repeated at least three times, for all the studied TMDs. The determined ε values (a mean of the three obtained values with standard deviation) were

6.4 ± 0.4, 1.2 ± 0.2, and 2.4 ± 0.1 mL·mg·cm^{-1} for MoS_2, WS_2, and $MoSe_2$, respectively. These values differ from those reported by other authors in the literature using the same quantification method.[94, 95] However, although the quantification method was the same, the exfoliation parameters were not. As such, the number of TMD layers as well as particle sizes are not the same, which greatly influences these results. This fact clearly highlights the importance of determining the values of ε under the specific processing conditions used.

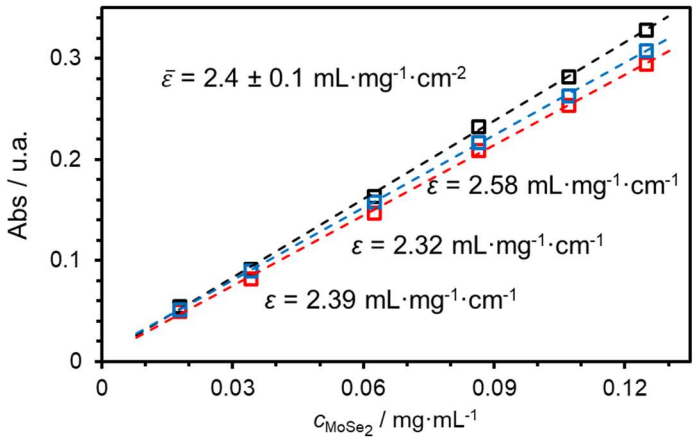

Figure 8 – Absorbance *vs.* concentration of dispersed $MoSe_2$ for the determination of ε.

2.2.2 Nanocomposites assembly

Figure 9 shows a schematic representation of the nanocomposites assembly process.

The assembly process begins with the preparation of two dispersions, by surfactant-assisted liquid phase exfoliation (SALPE), using the same procedure explained above and reported in ref.[92] 60 mg of the nanomaterial powder (MWNTs or TMDs) were added to 20 mL of a certain concentration of a surfactant aqueous solution (maintaining the 3 mg·mL^{-1} loading). For MWNTs, 5 mmol·kg^{-1} of TTAB surfactant aqueous solutions were used, while for TMDs, 10 mmol·kg^{-1} of SC surfactant aqueous solutions were used, corresponding to the surfactant concentrations at which maximum nanomaterial dispersibility is attained.

Both mixtures were then tip-sonicated, using a Sonics VC 505 with a freshly polished 13 mm tip (500 W, 20 kHz). For the TMD dispersions, vibration amplitude was set to 50%

and sonication time to 23 min, while for MWNT dispersions, the parameters were 60 % vibration amplitude and 5 min of time. These conditions were already optimized from previous work done in our research group [90-92] and were so that the energy transferred per unit mass were maintained for either material (0.20 kJ·mg^{-1} for MWNTs; 0.84 kJ·mg^{-1} for TMDs). An external bath was used to stabilize the temperature of the samples. Following sonication, MWNT dispersions were centrifuged (Centurion Scientific K241R) for 20 min at 4000 g. TMD dispersions were not centrifuged, as it was noted that the final nanocomposite materials had a very low concentration of TMDs should the TMD dispersions be centrifuged. The top of the supernatant (MWNTs dispersion) was collected and the final dispersions (both MWNTs and TMDs) were weighted.

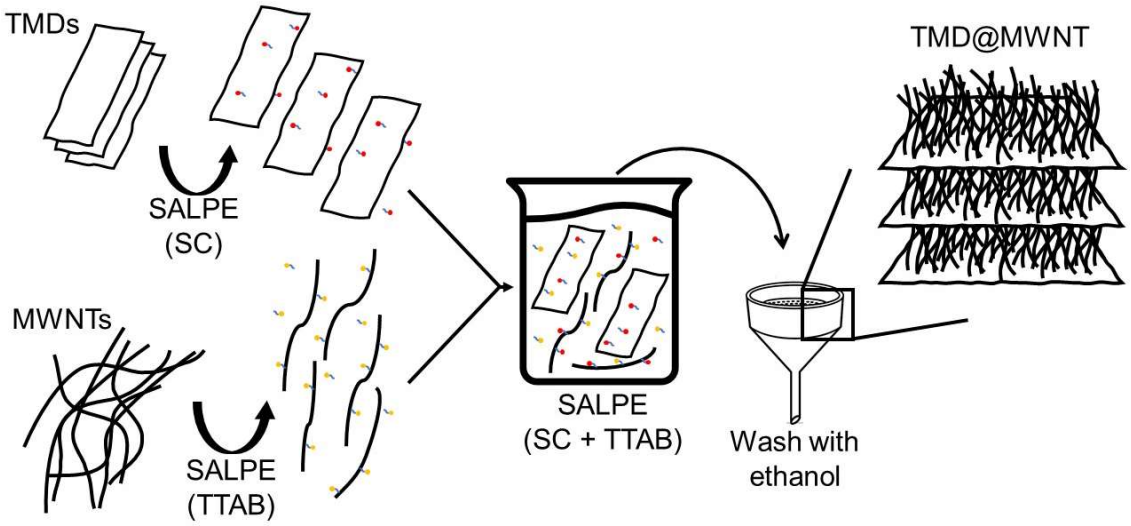

Figure 9 – Schematic representation of the TMD@MWNT nanocomposites assembly process.

The final exfoliated nanomaterial dispersions were mixed (either as-obtained, or using controlled amounts of each one, depending on the sample requirements) and sonicated using the same value of energy per mass used for MWNTs (0.20 kJ·mg-1). Because MWNTs can easily break under higher energy densities, this was the value set as maximum, since TMDs had a higher one (0.84 kJ·mg-1). As such, vibration amplitude was maintained at 60%, but sonication times varied according to the overall sample mass. After these processes, the samples were vacuum filtered, rinsed with ethanol and dried overnight.

2.3 Characterization methods

2.3.1 Ultraviolet-visible spectrophotometry (UV-Vis)

Ultraviolet-visible spectrophotometry (UV-Vis) is a widely used technique to quantify a large number of inorganic, organic and biological species.[96] When exposed to ultraviolet-visible radiation, valence electrons of these molecules absorb part of this radiation, transitioning to a superior energy state. The absorbed energy can be measured by the difference between emitted and received (after passing through the sample) radiation in a parameter called absorbance (*A*). It is linearly related to the concentration of the absorbing analyte being studied, as given by Lambert-Beer's law (equation (4)):[96]

$$A = \varepsilon l c \tag{4}$$

where ε is the molar extinction coefficient, l is the path length of the sample and c is the concentration of the analyte/species.

Experimental procedure. UV-Vis was used to evaluate the concentration of TMD present in the dispersions, after the SALPE process. 1 mL of the sample was transferred to a plastic cuvette (Brand) and 2 mL of ultrapure water was added to dilute the samples, so as not to exceed the absorbance value of 1. An Agilent 8453 spectrophotometer was used in all the measurements. The wavelengths at which absorbance was recorded differed between TMD, according to the material spectrum: 678 nm for MoS_2, 630 nm for WS_2 and 660 nm for $MoSe_2$.

2.3.2 Zeta potential (ζ)

Zeta potential (ζ) is the difference in potential between a particle and the solution where it is suspended in. It is observed at the slipping plane, the boundary region within which the particle behaves like a single entity. Zeta potential often relates to the colloidal stability of suspensions: higher potential differences at the surface of the suspended particles mean higher electrostatic repulsions between them and, consequently, a lower chance of aggregation and precipitation.[97, 98]

Zeta potential is not directly measured. Generally, the process of measuring this property involves applying an electric field to the dispersion. Suspended particles will be forced to move: negatively charged ones will move to the positively charged electrode and *vice-versa*.[98] The velocity of this movement is proportional to zeta potential, as shown in the known Henry equation (5):[99]

$$U_E = \frac{2\varepsilon_r \zeta}{3\mu} f(\kappa\alpha) \quad (5)$$

where U_E is the electrophoretic mobility, ε_r is the dielectric constant, μ is the medium viscosity and $f(\kappa\alpha)$ is the Henry function.

Experimental procedure. Zeta potential measures were carried out to assess the shelf life stability of the SALPE samples. Measurements were done using an Anton Paar Litesizer 500 particle size analyzer, with a 40 mW semiconductor laser (658 nm). All ζ values are mean values based on 2 independent dispersions (3 measurements per dispersion), using a ε_r value of 78.5, a μ value of 0.89 cP and a $f(\kappa\alpha)$ value of 1.5.[90]

2.3.3 Scanning electron microscopy (SEM)

SEM is a technique that allows for the determination of the morphology and topology of the surface of a sample. When an electron beam scans a material, it interacts with molecules on its surface, thus emitting several particles, namely secondary electrons, retro-diffused electrons and X-ray photons. Detectors inside the sample chamber analyze these radiations and build an image that varies the intensity of its color according to the sample's surface morphology and topology.[100]

Experimental procedure. SEM was employed in the characterization of these surface aspects of the studied materials. Sample preparation was done by dropcast, where a droplet of the prepared dispersions was dropped on a pre-heated flat silicon plate and the solvent was evaporated. Silicon plates were then rinsed with ethanol to remove the excess of surfactant. To analyze the cross section and deposition process of the nanocomposite materials, cellulose acetate membranes containing the still freshly deposited sample were dipped in liquid nitrogen, which allowed for cracks to be made.

These cracks correspond to the cross sections of the nanocomposite materials and could be analyzed with SEM.

SEM studies were performed in an environmental (low-vacuum) scanning electron microscope (Schottky) at *Centro de Materiais da Universidade do Porto* (CEMUP) operated at 15 kV for the TMDs and nanocomposites and at 25 kV for CNTs. Ampliation of the micrographs ranged from 5000x to 100000x. Size distribution of the individual TMDs was recorded and statistically analyzed (more than 50 objects were measured to ensure meaningful statistics).

2.3.4 Raman spectroscopy

Raman spectroscopy is used to find and characterize vibrational modes of a molecule. When a photon collides with a molecule and the resulting collision corresponds to a net change in energy, these are called inelastic collisions. These are Raman active, meaning they can be detected by a Raman spectrometer, and usually relate to symmetric vibrational modes. Thus, Raman spectroscopy provides a fingerprint of the molecule with emphasis on non-polar bonds, such as aromatic and carbon backbones.[101]

Experimental procedure. Raman spectroscopy primary objective was to determine the number of layers of the TMDs in the samples dispersed without surfactant and after the SALPE procedure. Raman spectra of the aqueous nanomaterial dispersions were recorded on a RAMOS RA532 Raman Analyzer using a laser emitting at 532 nm on glass cuvette, at room temperature.

2.4 Electrochemical techniques

An Autolab PGSTAT 302N potentiostat/galvanostat (EcoChimie B.V.), controlled by Nova v2.1 software was used to carry out all electrochemical studies. All studies were executed at room temperature and in a conventional three electrode cell setup: working electrode was a glassy carbon rotating disk electrode (RDE, Metrohm, diameter of 3 mm); reference electrode was Ag/AgCl (Metrohm, 3 mol·dm^{-3} $KCl_{(aq)}$); counter electrode was a carbon rod (Metrohm, diameter of 2 mm) for ORR studies, and a platinum wire (Goodfellow, diameter of 0.6 mm, l = 0.5 m, >99.99%) for OER studies.

The RDE was conditioned with a polishing process using diamond pastes (Buehler, MetaDI II) with three different particle sizes (6, 3 and 1 μm), before being modified with the samples. Modification of the electrode consists in dropping two 2.5 μL droplets of a dispersion containing the materials onto the glassy carbon surface of the RDE, and letting it dry under a constant flux of hot air. The dispersions used to modify the RDE were prepared by mixing 1 mg of the nanomaterial with 125 μL of isopropyl alcohol, 125 μL of ultrapure water and 20 μL of Nafion 117, followed by a 15 min bath ultrasonication (Fisherbrand FB11201).

2.4.1 ORR studies

All ORR studies used KOH (0.1 mol·dm^{-3}, 100 mL) saturated with oxygen or nitrogen gas as the electrolyte. To ensure proper saturation of the solution with the gas, the degassing process was maintained for at least 30 min prior to the study. N_2-saturated studies served as a blank for the O_2-saturated ones, and as such, current obtained in the first was subtracted to that obtained in the second. Electrocatalytic performance of the materials toward the ORR process was studied by cyclic voltammetry (CV) and linear sweep voltammetry (LSV). The scan rate for both was 5 mV·s^{-1}, and rotation speed for LSV was 400, 800, 1200, 1600, 2000 and 3000 rpm.

The E_{onset} vs. Ag/AgCl values were converted to E_{onset} vs. RHE (reversible hydrogen electrode), using equation (6).

$$E_{RHE} = E_{Ag/AgCl} + 0.059pH + E^0_{Ag/AgCl} \quad (6)$$

where E_{RHE} is potential vs. RHE; $E_{Ag/AgCl}$ is potential vs. Ag/AgCl; and $E°_{Ag/AgCl}$ = 0.1976 V (25 °C).

Onset potential, defined as the potential at which the reduction of O_2 begins, can be determined by different methods[8, 102] and is generally assumed as the potential at which the ORR current is 5% of the diffusion-limiting current density. Alternatively it can be calculated as the potential at which the slope of the voltammogram exceeds a threshold value (j = 0.1 mA cm^{-2}).[8, 102] Here we considered both methods.

To determine the number of electrons being transferred per O_2 molecule (n_{O_2}) with LSV data, the Koutecky-Levich (K-L) equation (eq. (7)) was used.

$$\frac{1}{j} = \frac{1}{j_L} + \frac{1}{j_k} = \frac{1}{B\omega^{1/2}} + \frac{1}{j_k} \quad (7)$$

where j is the measured current density; j_L is the diffusion-limiting current density; j_k is the kinetic current density; and ω is the angular velocity. B parameter is related to the diffusion-limiting current density as shown in equation (8).

$$B = 0.2 n_{O_2} F (D_{O_2})^{2/3} \upsilon^{-1/6} C_{O_2} \quad (8)$$

where F = 96485 C·mol^{-1}; D_{O_2} is the O_2 diffusion coefficient (1.95 × 10^{-5} cm^2·s^{-1} for this electrolyte); v is the electrolyte kinematic viscosity (8.977 × 10^{-3} cm^2·s^{-1}); and C_{O_2} is the bulk concentration of O_2 (1.15 × 10^{-3} mol·dm^{-3} in this electrolyte). For rotation speeds in rpm is adopted a constant of 0.2.

Methanol resistance and chronoamperometry studies were also carried. These were both done at a fixed potential of E = -0.55 V vs. Ag/AgCl and speed rotation or 1600 rpm. Methanol resistance study ran for 2500 s, at 500 s 2 mL of methanol was added to the electrolyte. Chronoamperometry lasted for 36000 s.

2.4.2 OER studies

OER studies were carried with KOH (0.1 mol·dm^{-3}, 100 mL) degassed with oxygen gas. These studies involved acquiring LSV polarization curves from 1.0 to 1.8 V vs. RHE, with a scan rate of 5 mV·s^{-1} and a speed rotation of 1600 rpm. Circuit uncompensated resistances (R_u) were estimated from *i*-interrupt tests, and 90% of R_u values were applied during the LSV tests for i_R-compensation.

Chapter 3

Results and Discussion

3 Results and Discussion

The dispersibility behavior of the studied TMDs in water, as well as the characterization of the starting materials and built TMD@MWNT nanocomposite materials, are presented in this chapter.

3.1 Dispersibility behavior of the starting materials

3.1.1 Dispersibility curves

Prior to the integration of each TMD (MoS_2, WS_2 and $MoSe_2$) in the assembly of the TMD@MWNT nanocomposites, their dispersibility behavior of was studied. The dispersibility curves obtained for MoS_2, WS_2 and $MoSe_2$ in aqueous SC and CTAB solutions are shown in Figure 10. These studies allowed the monitorization of the influence of the surfactant nature (anionic or cationic), as well as the influence of the metal and chalcogen moieties, in the dispersibility behavior of the TMDs. There are two noteworthy considerations: 1) the initial concentration of TMDs of 3 mg·mL^{-1} is constant in all systems; 2) the surfactant concentration, c_{surf}, is expressed in molality (specifically, surfactant amount in mmol per water mass in kg) and was varied between $1 \times 10^{-5} - 1 \times 10^{2}$ mmol·kg^{-1}.

Both anionic (SC) and cationic (CTAB) surfactants show similar dispersibility behaviors for MoX_2 materials, the difference being the presence of a “well” in the curve of the CTAB. When dispersed with SC, the concentration of MoX_2 tends to grow non-monotonically as the concentration of surfactant increases up to ca. 10 mmol·kg^{-1}. It then decreases abruptly at concentrations above 10 mmol·kg^{-1}. As for CTAB, concentrations of MoX_2 tend be roughly constant with low c_{surf}, then undergo a decrease with c_{surf} between $1 \times 10^{-3} - 1 \times 10^{-1}$ mmol·kg^{-1}, and then an increase again. There is also an abrupt decrease in the concentration of MoX_2 past the 10 mmol·kg^{-1} value for concentration of surfactant. This behavior in the dispersion curves (increase in concentration to a plateau) was already observed for other nanomaterials dispersed with different surfactants.[90-92] The sudden decrease in concentration after c_{surf} = 10 mmol·kg^{-1} may be due to an increase in the volume fraction of the micelles (since the concentration is above the *cmc* for both surfactants), which leads to aggregation and precipitation of the TMDs (due to osmotic depletion forces).[103]

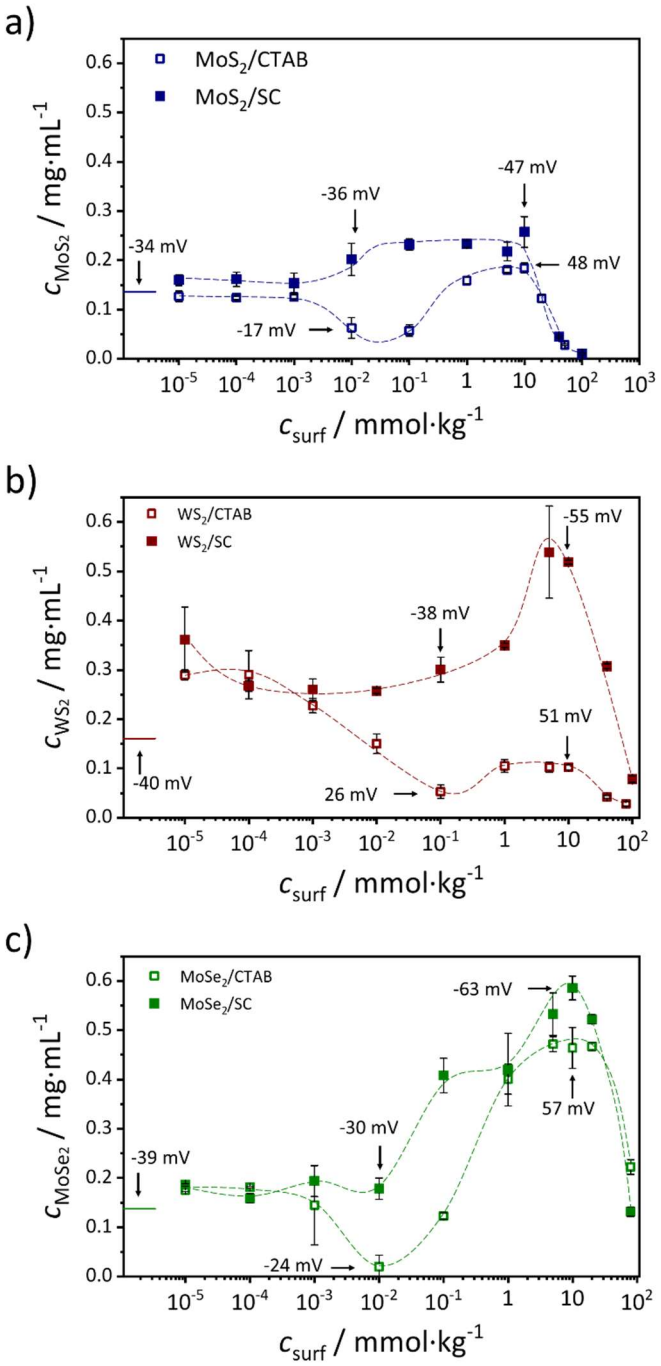

Figure 10 – Dispersibility curves of TMDs. Concentration of dispersed TMDs vs. concentration of surfactant (c_{surf}) in aqueous solution, in log scale: a) MoS_2 in SC and CTAB; b) WS_2 in SC and CTAB; c) $MoSe_2$ in SC and CTAB. Dashed lines are for visual guidance. Full lines indicate the concentration of TMD in water (no surfactant added). The insets show zeta potential values obtained for the samples indicated by the arrows.

The occurrence of the “well” in the CTAB dispersibility curves may be due to charge neutralization between MoX_2 and CTAB. The TMDs studied show a negative surface

charge (arrow insets in Figure 10), while CTAB is a cationic surfactant; thus, when the concentration of the surfactant is high enough, the charges cancel each other, and the TMD cannot be dispersed properly.

CTAB shows similar dispersibility at high concentrations for the MS_2 materials. While both MoS_2 and WS_2 show a peak concentration of 0.1 – 0.2 $mg \cdot mL^{-1}$ at higher c_{CTAB}, $MoSe_2$ has a peak concentration of 0.5 $mg \cdot mL^{-1}$. This suggests that the dichalcogenide influences dispersibility to a larger extent than the metal. Since the external layers of the 2D TMDs are composed of chalcogen atoms, this suggestion is reasonable from a structural point of view, as CTAB molecules bind non-covalently to the outer layer of the materials. However, the differences in the curves obtained for WS_2 suggest the metal also influences the dispersibility in water. The larger and heavier W atoms may interfere with surfactant-TMD interactions, resulting in a dispersibility curve with a different profile.

Results also show that TMDs can be dispersed in water. Zeta potential values reveal that the surface charge of the TMDs dispersed in water is negative. This ensures their ability to remain dispersed through the electrostatic repulsions that are established between the particles. These dispersions should not have high colloidal stability, as demonstrated by the module of zeta potential ($|\zeta|$) being close to 30 mV.[104]

Zeta potential results (arrow insets in Figure 10) give insight to the molecular mechanisms of the adsorption process. Surfactant molecules adsorb on the surface of the TMDs through their “tail”, exposing its polar “heads”.[105] In the case of dispersions with CTAB, this gradually changes the zeta potential charge from negative (TMDs dispersed in water) to a positive value (due to the exposed cationic polar “heads”). With SC dispersions, the increase in the $|\zeta|$ suggests that the anionic polar “heads” of the surfactant are, indeed, exposed.

3.1.2 Colloidal stability studies

The concentration and zeta potential of TMDs were monitored for 3 weeks, once a week, and using the same samples (left undisturbed), to assess the colloidal stability of the dispersions. Figure 11 shows the weekly variation of the c_{TMD} and module of zeta potential ($|\zeta|$) parameters.

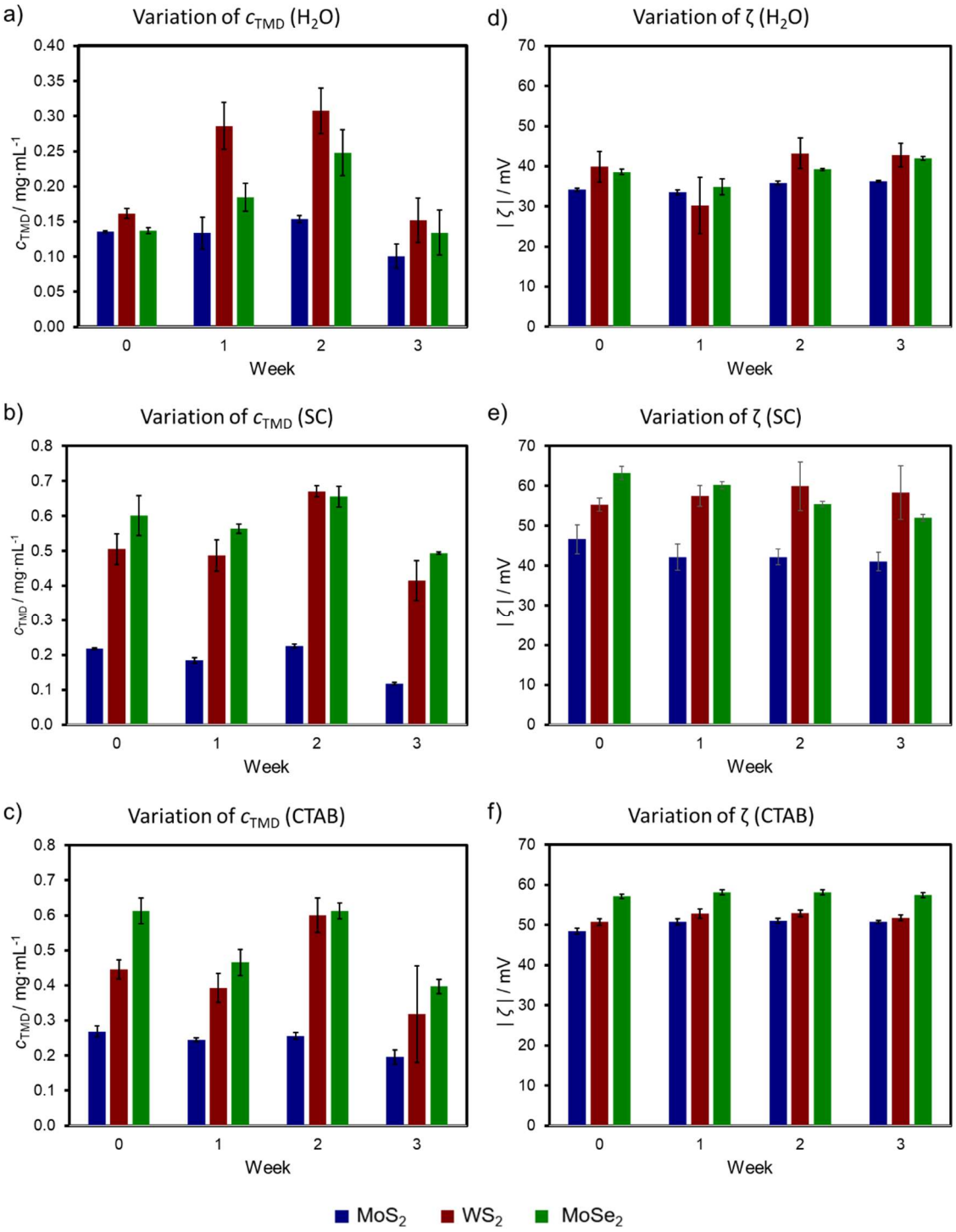

Figure 11 – Stability behavior of the studied TMDs: a) – c), weekly variation of c_{TMD} in neat H_2O, SC solution and CTAB solution, respectively; d) – f) weekly variation of | ζ | in neat H_2O, SC solution and CTAB solution, respectively.

Analyzing Figure 11 a) – c), the first remark is that the dispersions do not show long-term colloidal stability, since the values of c_{TMD} do not remain constant. Secondly, it is

important to note that a pattern can be observed for the dispersions with surfactants: in week 1 there is a decrease in c_{TMD}, followed by an increase in week 2, and finally another decrease in week 3. This unexpected non-monotonic variation may be due to two processes occurring simultaneously: aggregation and sedimentation of the TMD layers. In the first week, the larger TMD particles present from the original dispersion may start to sediment on the bottom of the flask, which causes a decrease in their concentration. However, in the second week, the smaller and still dispersed particles may start to aggregate and grow in size. This newly aggregated multi-layer particles may scatter the UV-Vis light of the spectrophotometer, resulting in a different ε value, leading to an apparent (and misleading) increase in the concentration of TMD. In the third week, the sedimentation process may again be the predominant one due to sufficient particle growth, resulting in the observed decrease in c_{TMD}.

The pattern observed for the dispersions with surfactant is different from the neat H_2O dispersion. With water, the concentration of TMDs in the dispersion increases in week 1 and 2 and decreases in week 3. Since a surfactant is not present to properly functionalize the TMD layers, these tend to aggregate more easily. As such, the aggregation process may start earlier than with the surfactant dispersions, resulting in the increase in c_{TMD}, explained by the abovementioned scattering phenomenon. Eventually, TMD particles may start to sediment which results in the decrease on c_{TMD} in week 3. This suggests that, albeit being metastable dispersions (and not true solutions in thermodynamic equilibrium), the surfactants present in the samples tend to avoid the inherent aggregation process of 2D layered materials.

Analyzing now Figure 11 d) – f), zeta potential does not vary significantly with time for all the systems investigated. This is possible indicative that whichever the size variation of the particles with time, the degree of surface coverage by the ionic surfactants does not change appreciably, resulting in near unchanged zeta potential. This constancy of zeta potential with time is especially seen in the case of the CTAB dispersions. This may have to do with the different charges of the materials, anionic TMDs and cationic CTAB.

3.2 Characterization of materials

3.2.1 Characterization of TMDs

Bulk MoS_2, WS_2 and $MoSe_2$ without any changes were characterized by SEM and representative micrographs are shown in Figure 12. These micrographs very distinctively allow the characterization of the samples as 2D nanomaterials containing layered sheets. WS_2 stands out because of the very defined sheet edges, with an almost hexagonal-like shape. MoX_2 TMDs show more undefined edges, roughly scattered through the sample, which indicates the metal plays a larger role on the morphology of the surface of these materials.

Besides the bulk solid materials, aqueous dispersions of the TMDs in neat H_2O, in SC and in CTAB were also studied by SEM (Figure 13). Particle aggregates or clusters can more easily be observed in neat H_2O dispersions. Surfactant aqueous dispersions tend to show more single particles or smaller aggregates, as a consequence of the interactions between surfactants and TMDs.

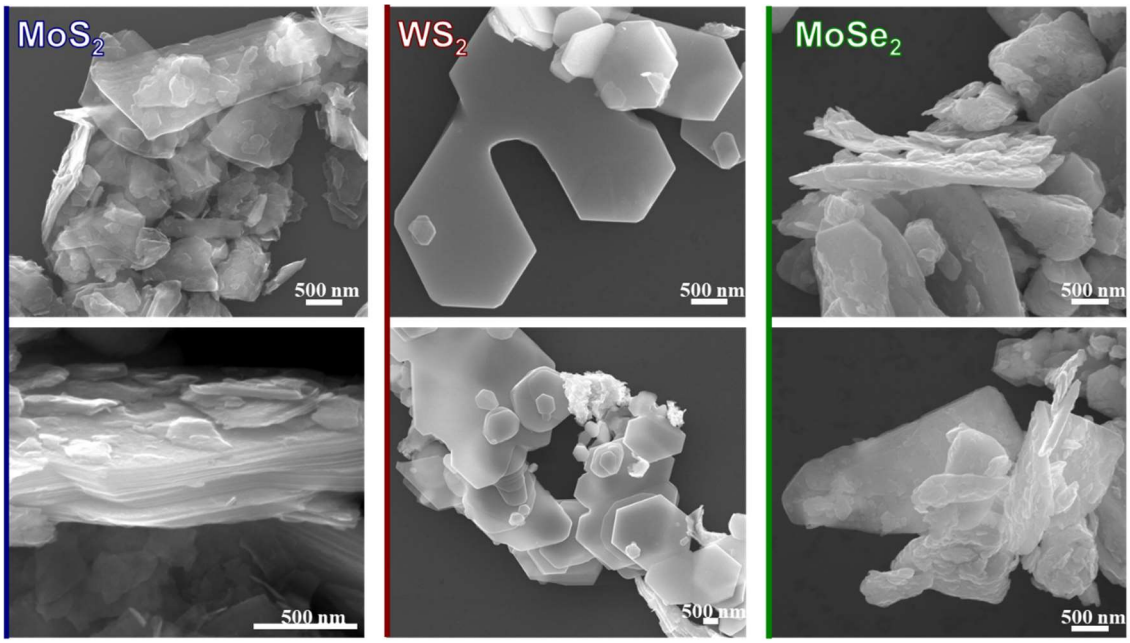

Figure 12 – SEM micrographs of bulk MoS_2, WS_2 and $MoSe_2$.

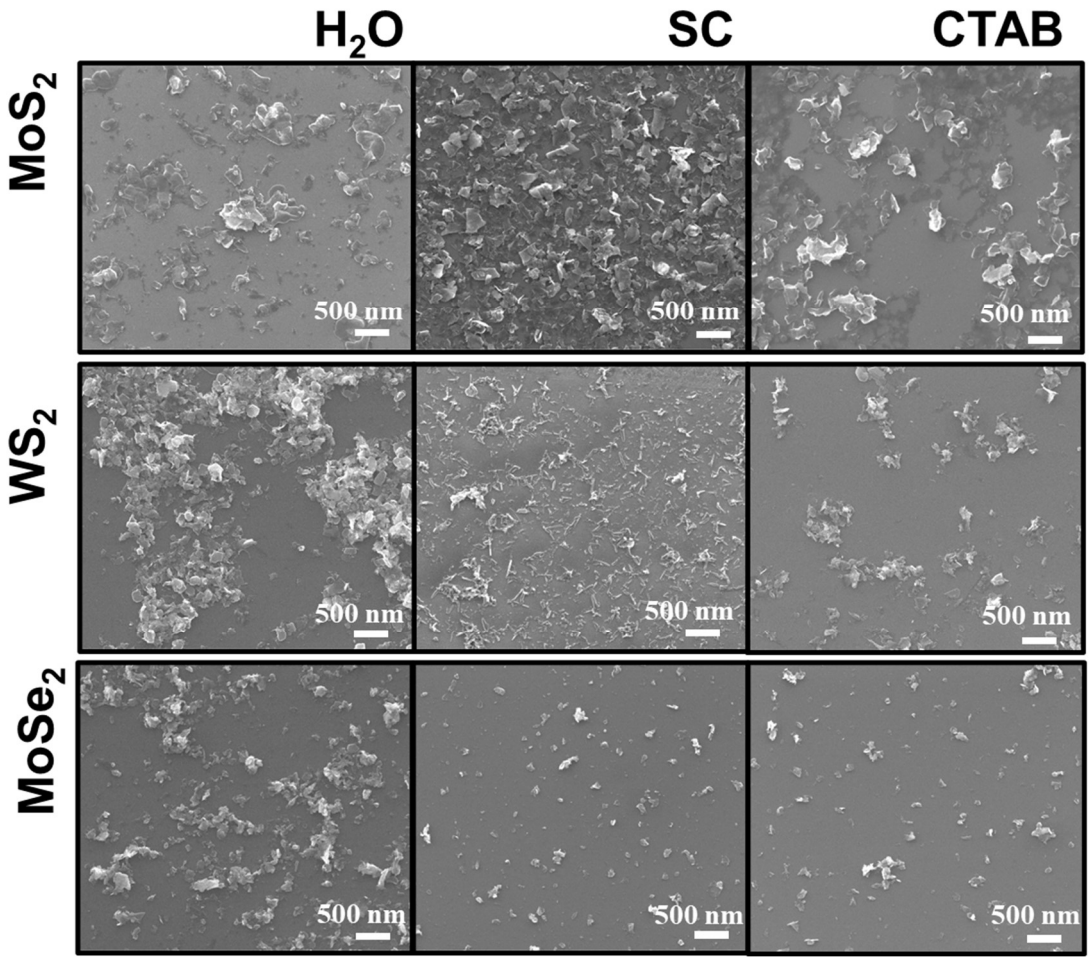

Figure 13 – SEM micrographs of MoS_2, WS_2 and $MoSe_2$ dispersed in H_2O, and SC and CTAB aqueous solutions.

In addition, SEM studies on the dispersed nanomaterials allowed the measurement of the mean lateral dimension (*MLD*) of single layers. Histograms of these dimensions are presented in Figure 14. The histograms of the *MLD* of the particles were fitted to a log-normal distribution, according to equation (9):

$$P(L) = \frac{1}{\sqrt{(2\pi)wL}} e^{\frac{-\left[ln\left(\frac{L}{L_m}\right)\right]^2}{2w^2}} \quad (9)$$

where L_m is the median of *MLD* measurements and *w* is the width of the log-normal curve (this parameter accounts for polydispersity of the $\overline{MLD}$). The mean of the *MLD* distribution is given by equation (10):

$$\overline{MLD} = L_m e^{\frac{w^2}{2}} \quad (10)$$

Analysis of the histograms show that dispersions with CTAB have less variations in the dimensions, with log-normal distributions being less polydisperse. Once again, this may be due to the different charges in the TMD and the surfactant, causing less variation in the $\overline{MLD}$ of the particles after the exfoliation process.

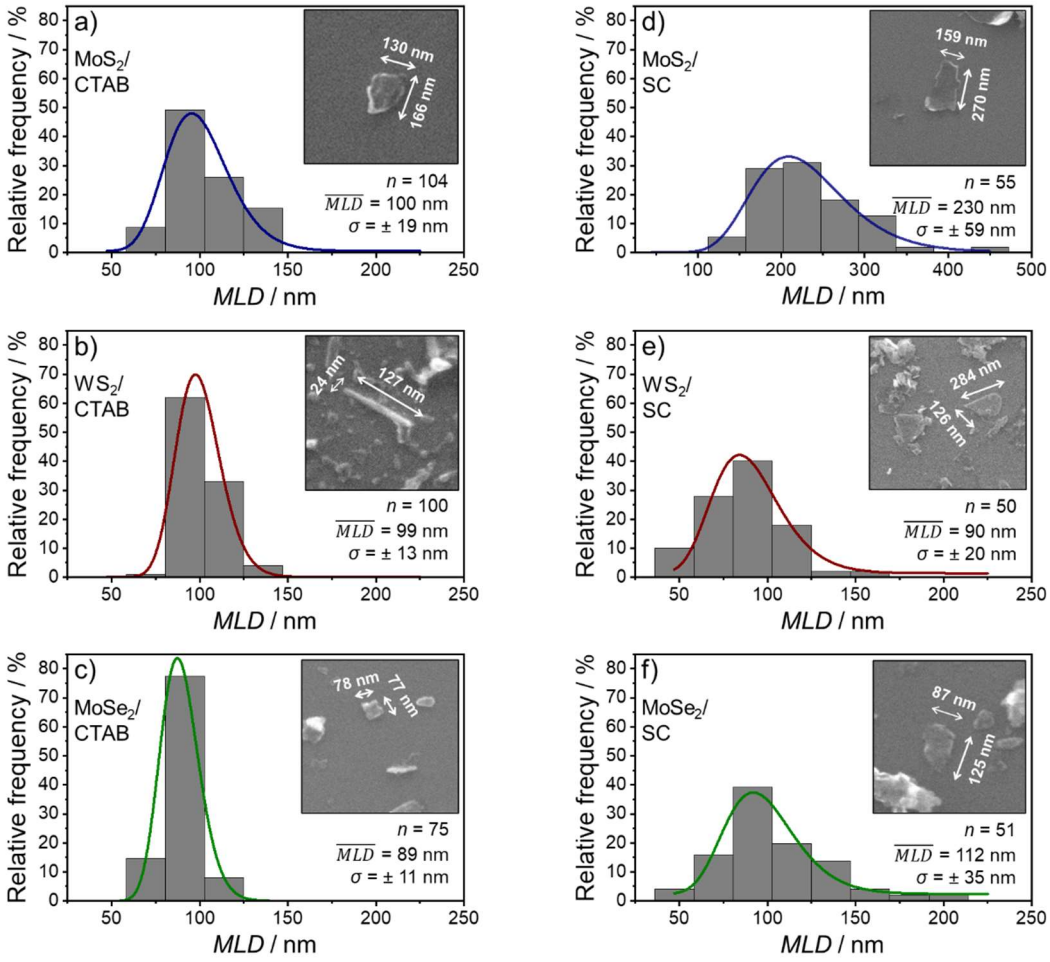

Figure 14 – Histograms of the mean lateral dimensions of a) MoS_2 in CTAB, b) WS_2 in CTAB, c) $MoSe_2$ in CTAB, d) MoS_2 in SC, e) WS_2 in SC, and d) $MoSe_2$ in SC. The insets show a representation of the measurement method. Histograms were fitted to a log-normal distribution. The mean, $\overline{MLD}$, and width, σ, of the distribution are shown, as well as the number of counts (*n*).

Figure 15 shows the Raman spectra obtained for the TMDs dispersed in neat H_2O, in SC and in CTAB solutions. These studies were carried to further investigate the properties of the TMD materials. Two peaks can be observed, one concerning the E_{2g} (in-plane) vibration mode, and another the A_{1g} (out-of-plane) vibration mode. The exfoliation of TMDs affects Raman shifts: generally, E_{2g} and A_{1g} modes undergo blue (shift to higher wavenumbers) and red (shift to lower wavenumbers) shifts with decreasing numbers of layers, respectively.[106-108]

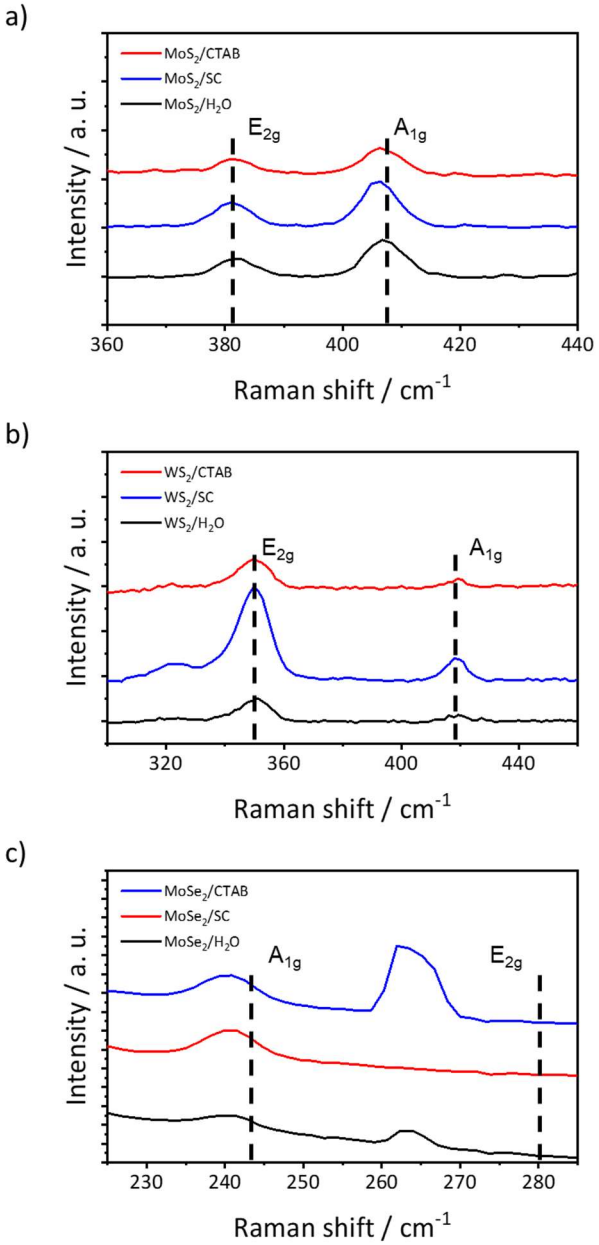

Figure 15 – Raman spectra (obtained with a green laser at 532 nm) for a) MoS_2 dispersions; b) WS_2 dispersions, and c) $MoSe_2$ dispersions. Dashed lines represent expected A_{1g} and E_{2g} peaks for monolayer MoS_2[109], WS_2[110], and $MoSe_2$[111].

Results show that the dispersions contain few-layer TMDs. Particularly, MoS_2 and WS_2 are very close to being monolayers. However, $MoSe_2$ spectra show that the E_{2g} mode undergoes an evident red shift. The expected upshift of E_{2g} with decreasing thickness is assigned to a decrease in magnitude of the long-range electrostatic forces between particles. In. fact, as the number of layers is reduced, electrostatic forces between the charged particles become weaker.[109, 110, 112] The observed downshift of the E_{2g} mode in $MoSe_2$ may be due to interactions between the Se outer-layer of the nanosheets and the surfactant. This is further evidenced by the $MoSe_2$/CTAB Raman spectra: since there are now attractive electrostatic forces between the positively-charged CTAB and negatively-charged $MoSe_2$, the magnitude of electrostatic forces increase, resulting in the observed downshift of the E_{2g} mode.

3.2.2 Characterization of the carbon nanocomposites

Nanocomposite materials comprised of pre-exfoliated TMDs (WS_2 and MoS_2) with SC and pre-exfoliated MWNTs with TTAB were assembled via the method described in chapter 2.2.2. The resulting nanomaterials (WS_2@MWNT and MoS_2@MWNT) were characterized by SEM. Figure 16 and Figure 17 show some representative micrographs of the WS_2@MWNT and MoS_2@MWNT, respectively.

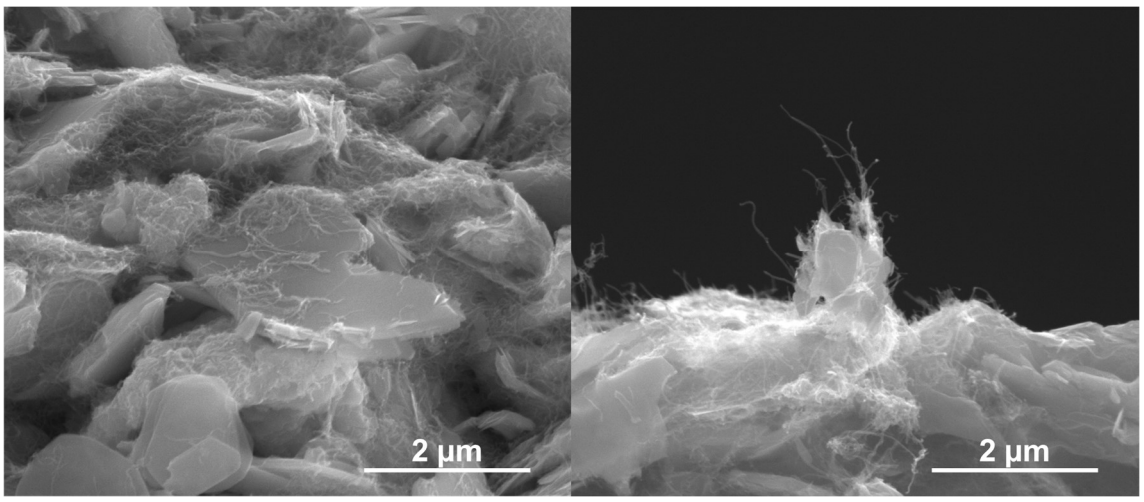

Figure 16 – SEM micrographs of WS_2@MWNT (50000x magnification).

Micrographs show a heterogeneous mixture of the TMDs and the MWNTs. As expected, MWNTs occupy the interstices of the TMD layers. Beyond that, the

micrographs show that the MWNTs adhere horizontally to the plane of the TMD layers. This suggests that, when placed on the glassy carbon electrode, MWNTs may serve as a wedge to the TMD sheets, forcing the edges to be exposed. This helps the electrocatalytic process, since the catalytic activity of TMDs arises from its chalcogen edges.[62]

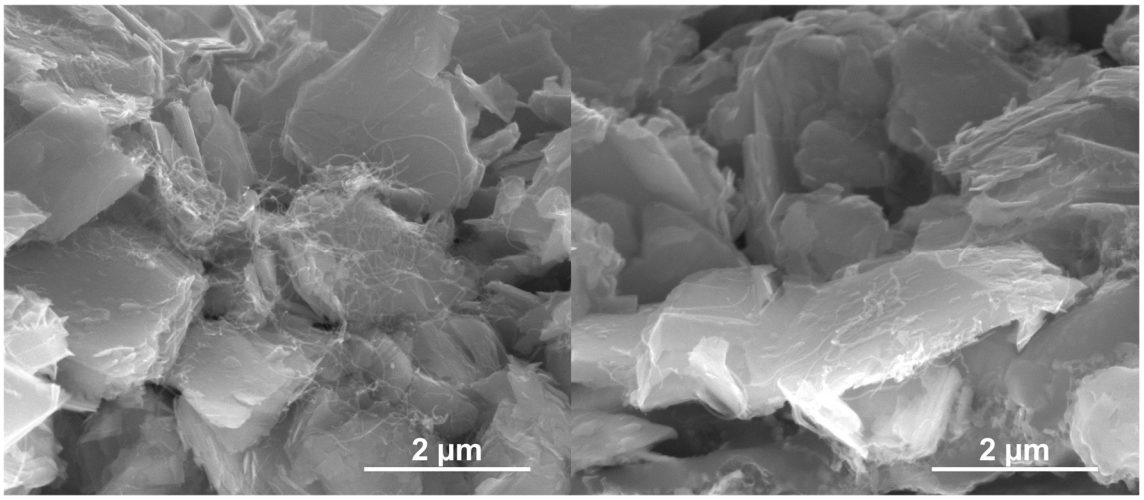

Figure 17 – SEM micrographs of MoS_2@MWNT (50000x magnification).

One major difference between the two TMD nanocomposites is the amount of MWNT that covers the surface of the 2D material. With WS_2@MWNT, MWNT bundles cover a large part of the WS_2 sheets, while on MoS_2CNT the opposite occurs, and MoS_2 sheets are more exposed. This may lead to different electrocatalytic activities, as the edges of the TMD sheets have different levels of exposure.

3.3 Electrocatalytic performance of the materials

3.3.1 Electrocatalytic activities of WS_2

3.3.1.1 ORR activity performance

The ORR electrocatalytic performances of pristine WS_2, WS_2/SC, MWNT/TTAB and WS_2@MWNT were initially evaluated by cyclic voltammetry (CV), in N_2 and O_2-saturated 0.1 mol·dm^{-3} KOH solution. The results are shown in Figure 18.

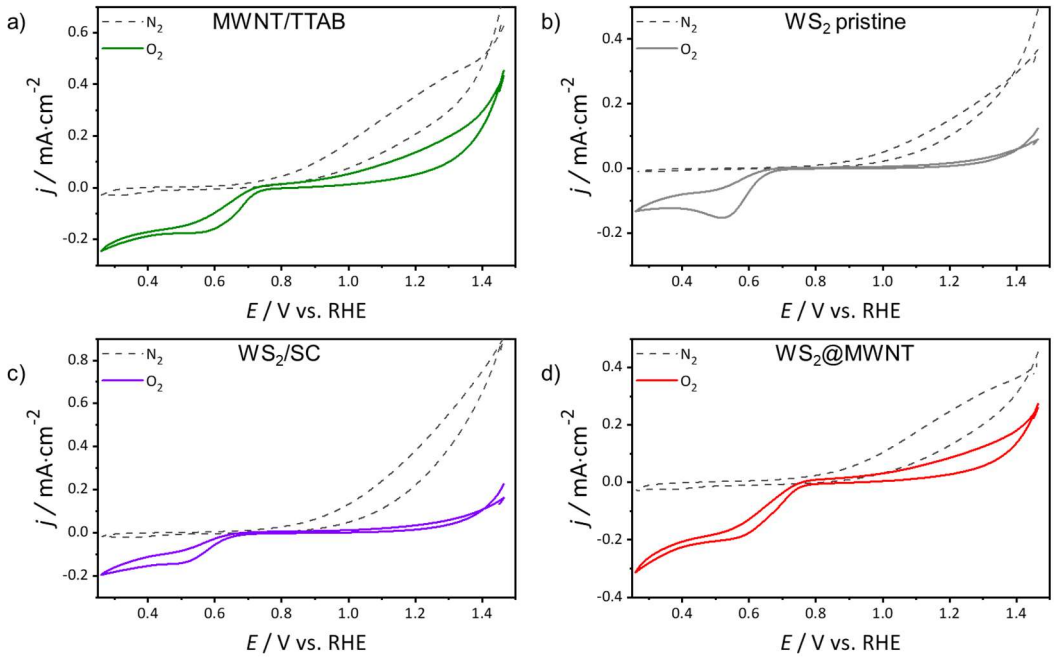

Figure 18 – CVs of a) MWNT/TTAB, b) WS_2 pristine, c) WS_2/SC, and d) WS_2@MWNT obtained in N_2- (dashed line) and O_2-saturated (full line) 0.1 mol·dm^{-3} KOH solution, at v = 0.005 V·s^{-1}.

In the N_2-saturated electrolyte solution none of the studied materials show electrochemical processes in the potential window studied. In contrast, in the O_2-saturated electrolyte, an ORR peak can be distinguished for all the materials. This peak occurs at E_{pc} = 0.58, 0.50, 0.52, and 0.58 V vs. RHE for MWNT/TTAB, WS_2 pristine, WS_2/SC, and WS_2@MWNT, respectively. This confirms the electrocatalytic activity of the materials toward the ORR. Figure 19 a) shows the CVs in O_2-saturated KOH for

MWNT/TTAB, WS_2 pristine, WS_2/SC, WS_2@MWNT and the benchmark electrocatalyst Pt/C. It can be clearly seen that the obtained results are still somewhat far from that obtained for Pt/C (E_{pc} = 0.86 V).

To unfold the kinetics of the ORR of the materials, linear sweep voltammetry (LSV) studies were carried in a N_2- and O_2-saturated electrolyte solution (0.1 mol·dm^{-3} KOH), at different rotation speeds (400 – 3000). The LSVs at 1600 rpm for all the materials are presented in Figure 19-b). From the LSV curves, onset potential (E_{onset}), current densities (j_L), and the number of electrons transferred per O_2 molecule (n_{O2}) parameters were obtained and are represented in Table 2. WS_2 pristine and WS_2/SC showed no significant differences, suggesting that the SALPE process did not alter their electrochemical performance towards ORR. The incorporation of MWNTs in the nanocomposite successfully increased the ORR activity of WS_2. Additionally, the values obtained for WS_2@MWNT (E_{onset} = 0.71 V vs. RHE and j_L = -1.87 mAcm^{-2}) were significantly far from those obtained for the Pt/C electrocatalyst (E_{onset} = 0.93 V vs. RHE and j_L = -4.15 mAcm^{-2}).

The number of electrons transferred per O_2 molecule was estimated through equations (7) and (8). All materials show a n_{O2} value close to 2 electrons, suggesting that the reaction occurs via the 2-electron indirect mechanism, which is not optimal. Figure 19-c) shows the n_{O2} values at different potentials for all the materials tested. It can be observed that for Pt/C and WS_2 pristine materials, the n_{O2} values are independent of the applied potential. This is not true for MWNT/TTAB and WS_2@MWNT, that show a decrease in n_{O2}, and for WS_2/SC, that show an increase in n_{O2} as the potential increases. This means that, for these materials, the process is dependent on the applied potential.

Table 2 – ORR activity parameters (E_{onset}, j_L, and n_{O_2}) for MWNT/TTAB, WS_2 pristine, WS_2/SC, WS_2@MWNT, and Pt/C samples.

Sample	**E_{onset} / V vs. RHE** (5% of j_{max})	**E_{onset} / V vs. RHE** (j = 0.1 mA·cm^{-2})	**j_L / mA·cm^{-2}**	**n_{O_2}**
MWNT/TTAB	0.68	0.68	-2.07	2.13
WS_2 pristine	0.62	0.60	-1.27	2.09
WS_2/SC	0.61	0.57	-0.94	2.36
WS_2@MWNT	0.71	0.70	-1.87	2.41
Pt/C	0.93	0.96	-4.15	3.44

Tafel plots (Figure 19-d)) were obtained from LSV data in Figure 19-b) at 1600 rpm, in O_2-saturated KOH. The ORR process exhibits Tafel slopes of 74, 76, 98, 74 and 110 mV·dec^{-1} for MWNT/TTAB, WS_2 pristine, WS_2/SC, WS_2@MWNT and Pt/C, respectively. These results suggest that for MWNT/TTAB, pristine WS_2 and WS_2@MWNT the global reaction rate is ruled by the conversion of MOO- (intermediate surface adsorbed specie) to MOOH (M is an empty site on the electrocatalyst surface) while for the other two (WS_2/SC and Pt/C) most likely the rate is determined by the first discharge step or the upon consumption of the MOOH species.[113]

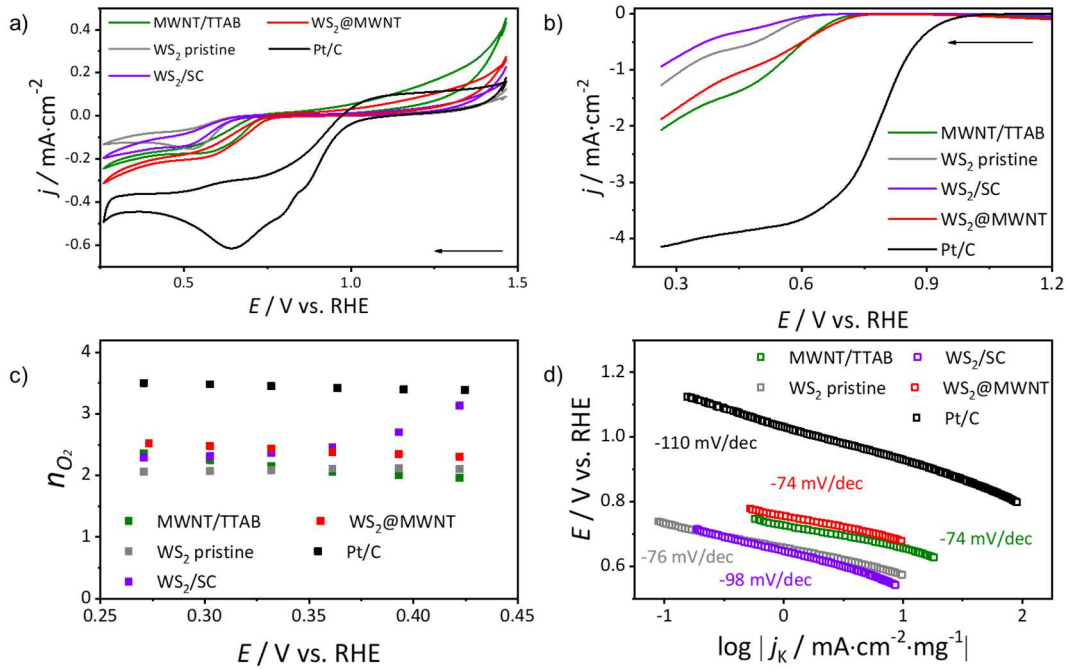

Figure 19 – Electrochemical studies on Pt/C, WS_2@MWNT nanocomposite, and its building blocks, WS_2 pristine, WS_2/SC and MWNT/TTAB. a) CVs (O_2-saturated 0.1 mol·dm^{-3} KOH, v = 0.005 V·s^{-1}); b) LSVs at 1600 rpm (O_2-saturated 0.1 mol·dm^{-3} KOH, v = 0.005 V·s^{-1}); c) n_{O2} at different potentials; d) Tafel plots.

3.3.1.2 OER activity performance

The electrocatalytic performance of these materials towards the OER was also evaluated. For that, LSV studies were carried, in a O_2-saturated 0.1 mol·dm^{-3} KOH electrolyte, at a scan rate of v = 0.005 V·s^{-1} and at 1600 rpm. The polarization curves

obtained are presented in Figure 20. As for ORR, the results were benchmarked using, in this case, one of the state-of-the-art OER electrocatalysts (RuO_2).

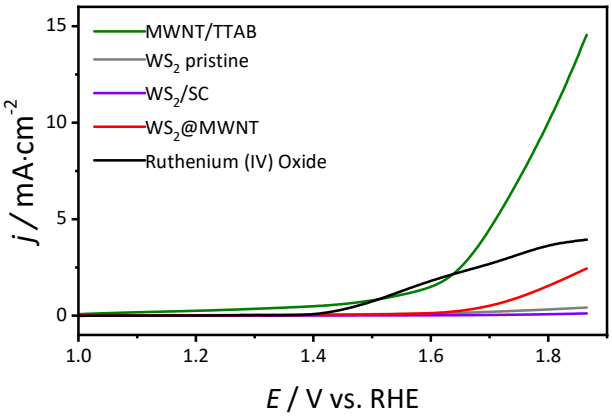

Figure 20 – OER polarization curves obtained by LSV (O_2-saturated 0.1 mol·dm^{-3} KOH, v = 0.005 V·s^{-1}, 1600 rpm) for MWNT/TTAB, WS_2 pristine, WS_2/SC, WS_2@MWNT and RuO_2.

Table 3 collects the OER activity parameters, derived from the LSV plots. Because current densities (j) do not exceed 10 mA·cm^{-2} for all the samples except MWNT/TTAB, overpotential values (η) were only possible for this material. To compare the results, $j_{1.8}$ was acquired, and it is the j value at a fixed potential of E = 1.8 V vs. RHE.

Table 3 – OER activity parameters (η, j_{max}, and $j_{1.8}$) for MWNT/TTAB, WS_2 pristine, WS_2/SC, WS_2@MWNT, and RuO_2.

Sample	**η / V** (j = 10 mA·cm^{-2})	**j_{max} / mA·cm^{-2}**	**$j_{1.8}$ / mA·cm^{-2}**
MWNT/TTAB	0.59	14.55	10.15
WS_2 pristine	----	0.42	0.32
WS_2/SC	----	0.12	0.076
WS_2@MWNT	----	2.45	1.57
RuO_2	----	3.94	3.64

Pristine WS_2, and WS_2/SC are definitely the materials with the poorest OER activity of the lot, with current densities maxing at 0.42 and 0.12 $mA \cdot cm^{-2}$, respectively. This indicates that these materials do not have the ability to promote the reaction envisaged. As a consequence, WS_2@MWNT did not show a good OER activity either, with a j_{max} = 2.45 $mA \cdot cm^{-2}$. On the other hand, MWNT/TTAB showed a good current density value, but at a reasonably high overpotential of η = 0.59 V. Regarding the benchmark material, RuO_2, its polarization curves show much lower current density than expected. Comparing the benchmark material to the nanocomposites is not recommended, since these materials have very different structures, and normalization of the polarization curves to their corresponding electrochemical active surface areas is advised.

3.3.2 Electrocatalytic activities of MoS_2

3.3.2.1 ORR activity performance

Since the WS_2@MWNT nanocomposite did not show a good electrocatalytic performance towards the oxygen reactions, a new nanocomposite of similar constituents, MoS_2@MWNT, was assembled and tested. It was studied by CV, in 0.1 $mol \cdot dm^{-3}$ KOH solution, saturated in N_2 and O_2. Pristine MoS_2, MoS_2/SC, and centrifuged MoS_2/SC (MoS_2/SC w/CF) were also evaluated. The latter material was studied to further investigate the impact of the centrifugation step in the preparation of the materials, since, as explained above, this step was omitted in the assembly of the nanocomposites due to practical reasons. The CVs of all materials are presented in Figure 21.

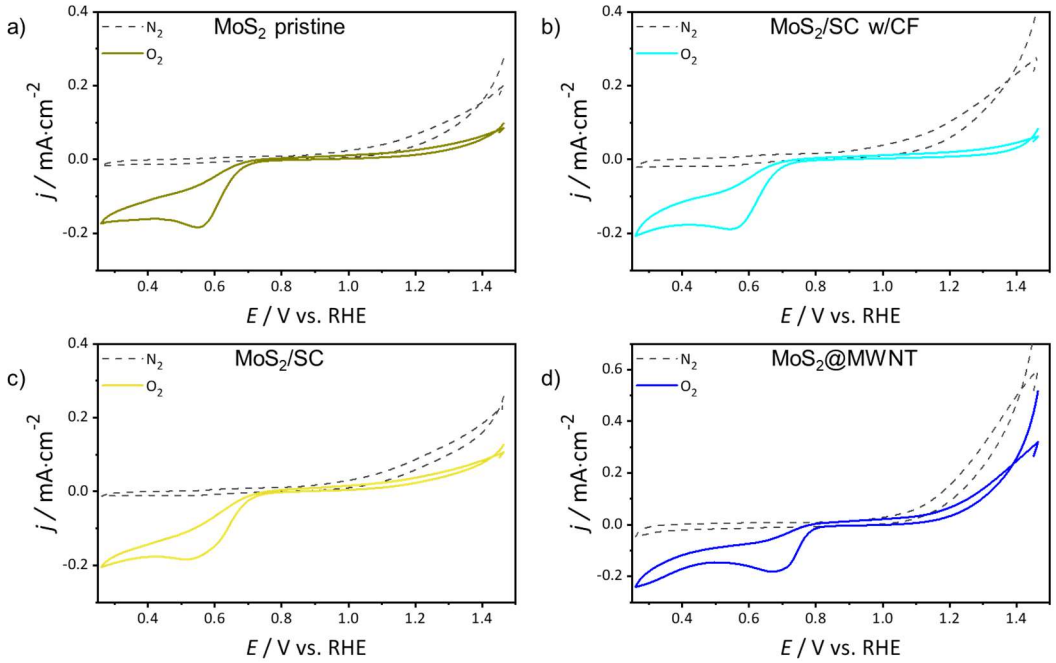

Figure 21 – CVs of a) MoS_2 pristine, b) MoS_2/SC w/CF, c) MoS_2/SC, and d) MoS_2@MWNT obtained in N_2- (dashed line) and O_2-saturated (full line) 0.1 mol·dm^{-3} KOH solution, at v = 0.005 V·s^{-1}.

The studied materials do not show electrochemical processes in N_2-saturated electrolyte solution in the potential window used. Contrastingly, an ORR peak can be distinguished for all the materials in the O_2-saturated electrolyte at E_{pc} = 0.54, 0.55, 0.55, and 0.72 V vs. RHE for MoS_2 pristine, MoS_2/SC w/CF, MoS_2/SC, and MoS_2@MWNT, respectively. These results confirm the ORR electrocatalytic activity of the materials. The nanocomposite showed an improvement in the E_{pc} parameter, suggesting the existence of a synergic interaction between the TMDs and the MWNTs. A comparison between the CVs of these materials, as well as Pt/C, is presented in Figure 22 – a).

LSV studies were carried in a N_2- and O_2-saturated electrolyte solution (0.1 mol·dm^{-3} KOH) at different rotation speeds (400 – 3000). Figure 22 – b) shows the resulting LSVs at 1600 rpm. ORR activity parameters (E_{onset}, j_L, and n_{O2}) were obtained from these curves and are presented in Table 4. MoS_2@MWNT activity was better than the WS_2@MWNT (E_{onset} = 0.73 V vs. RHE and j_L = -2.74 mA·cm^{-2}). These values were still significantly far from those obtained for the benchmark Pt/C electrocatalyst. MoS_2 pristine, MoS_2/SC w/CF, and MoS_2/SC show very similar results, as observed before for the WS_2 family of materials. This suggests that the centrifugation step is not crucial to the performance of the materials as electrocatalysts. Recent studies in the literature[31, 33]

show that the activity of MoS_2 towards the HER is enhanced when the surfactant is not present. However, this is not the case with ORR, as our results show. Nonetheless, in the final step of the assembly process, the nanocomposites were rinsed with ethanol to remove the excess surfactant.

As above, the n_{O2} values were estimated. Contrary to WS_2 materials, MoS_2 materials have n_{O2} values that are close to 3. This suggests that the reaction occurs via a mixed 2- and 4- electron mechanism. Although not optimal these are promising results, as further development may lead to an exclusive 4-electron reaction path. In Figure 22 – c), the n_{O2} values at different potentials plot are presented. It shows that all studied materials (except Pt/C) act through a process that is dependent on the applied potential, as illustrated by the variation of n_{O2} values with the potential.

Table 4 – ORR activity parameters (E_{onset}, j_L, and n_{O2}) for MWNT/TTAB, MoS_2 pristine, MoS_2/SC w/CF, MoS_2/SC, MoS_2@MWNT, and Pt/C samples.

Sample	E_{onset} **/ V vs. RHE** (5% of j)	E_{onset} **/ V vs. RHE** (j = 0.1 mA·cm^{-2})	j_L **/ mA·cm^{-2}**	n_{O2}
MWNT/TTAB	0.68	0.68	-2.07	2.13
MoS_2 pristine	0.63	0.62	-1.63	3.25
MoS_2/SC w/CF	0.64	0.63	-1.51	3.20
MoS_2/SC	0.64	0.63	-1.90	2.81
MoS_2@MWNT	0.73	0.74	-2.74	2.87
Pt/C	0.93	0.96	-4.15	3.44

Figure 22 – d) shows the Tafel plots for the different materials, obtained from LSV data in Figure 22 – b), at 1600 rpm in O_2-saturated KOH. The ORR process shows Tafel slope (*TS*) values of 74, 83, 78, 84, 49 and 110 mV·dec^{-1} for MWNT/TTAB, MoS_2 pristine, MoS_2/SC w/CF, MoS_2/SC, MoS_2@MWNT and Pt/C. These data suggest that for all MoS_2 materials the global reaction rate is ruled by the conversion of MOO- (intermediate surface adsorbed specie) to MOOH (M is an empty site on the electrocatalyst surface).[113]

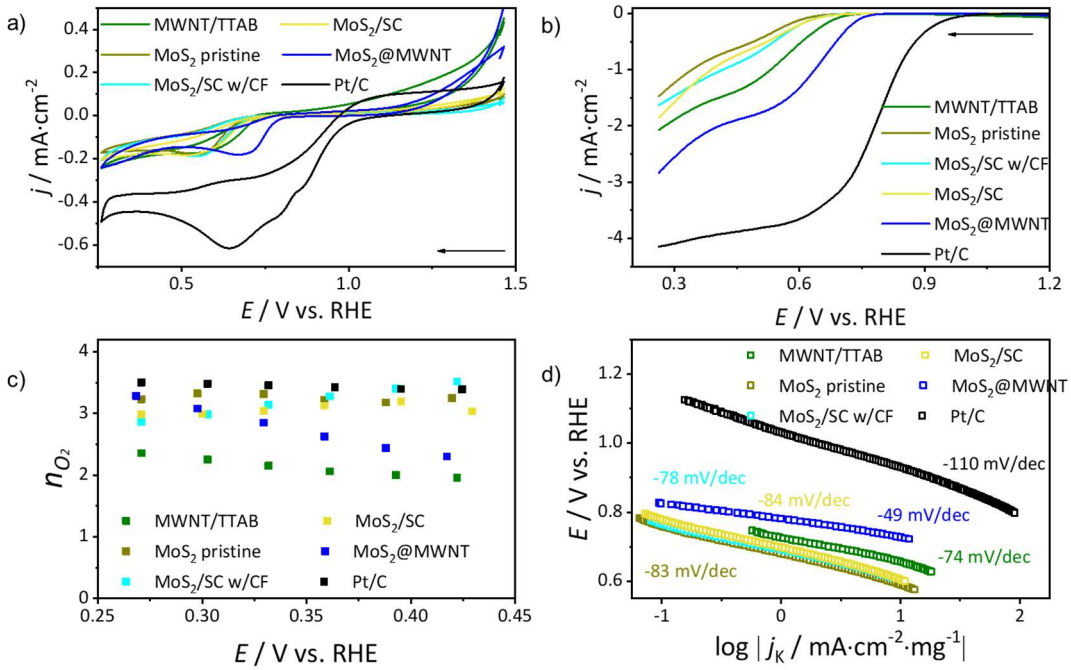

Figure 22 – Electrochemical studies on Pt/C, MoS_2@MWNT nanocomposite, and its building blocks, MoS_2 pristine, MoS_2/SC w/CF, MoS_2/SC, and MWNT/TTAB. a) CVs (O_2-saturated 0.1 mol·dm^{-3} KOH, v = 0.005 V·s^{-1}); b) LSVs at 1600 rpm (O_2-saturated 0.1 mol·dm^{-3} KOH, v = 0.005 V·s^{-1}); c) n_{O2} at different potentials; d) Tafel plots.

Since the MoS_2@MWNT nanocomposite showed promising results, attempts at further developing these materials were made by assembling MoS_2@MWNT nanocomposites with variable TMD:MWNT mass ratios, namely MoS_2@MWNT (1:1), MoS_2@MWNT (1:3), and MoS_2@MWNT (3:1). Further, a MoS_2@N-MWNT nanocomposite, comprised of layered MoS_2 and N-doped multiwalled carbon nanotubes was also built to assess the effect of doping the MWNT on the electrocatalytic efficiency towards ORR. The results regarding these new materials are shown in Figure 23 – a) and b), and Table 5 presents the ORR parameters evaluated (E_{onset}, j_L, and n_{O2}).

Results indicate that there is no significant difference in the electrocatalytic activity towards the ORR. E_{onset} values vary, not significantly, from 0.73 to 0.72 V vs. RHE, for MoS_2@MWNT (1:3) and MoS_2@MWNT (3:1), and j_L varies from -2.46 to -2.92 mA·cm^{-2}, for MoS_2@MWNT (1:3) and MoS_2@MWNT (3:1). There is, also, a slight increase in n_{O2} values, from 2.34 to 2.73 for MoS_2@MWNT (1:3) and MoS_2@MWNT (3:1), but this is not significant. As such, there is no apparent best performing material. This suggests that the ORR activity of the material is independent of the ratio between MoS_2 and MWNT,

or that there is too small of a difference between the different ratios studied. MoS_2@MWNT is still the nanocomposite with slightly better ORR activity.

Table 5 – ORR activity parameters (E_{onset}, j_L, and n_{O2}) for MoS_2@MWNT, MoS_2@MWNT (1:1), MoS_2@MWNT (1:3), MoS_2@MWNT (3:1), and MoS_2@N-MWNT samples.

Sample	E_{onset} **/ V vs. RHE** (5% of j)	E_{onset} **/ V vs. RHE** (j = 0.1 mA·cm^{-2})	j_L **/ mA·cm^{-2}**	n_{O2}
MoS_2@MWNT	0.73	0.74	-2.74	2.87
MoS_2@MWNT (1:1)	0.73	0.73	-2.47	2.37
MoS_2@MWNT (1:3)	0.73	0.73	-2.46	2.34
MoS_2@MWNT (3:1)	0.72	0.73	-2.92	2.73
MoS_2@N-MWNT	0.74	0.75	-2.50	2.66

Tafel plots (Figure 23– c)) and n_{O2} in function of the applied potential plot (Figure 23 – d)) were also obtained from LSV data at 1600 rpm, in O_2-saturated KOH.The ORR process showed TS of 49, 53, 55, 54 and 50 mv·dec^{-1} for MoS_2@MWNT, MoS_2@MWNT (1:1), MoS_2@MWNT (1:3), MoS_2@MWNT (3:1) and MoS_2@N-MWNT. Just as with the other MoS_2 materials, the hypothesis is that the global reaction rate is ruled by the conversion of MOO- to MOOH.[113] Dependance of n_{O2} on the applied potential was found for all MoS_2 family nanocomposites.

Interestingly, MoS_2@N-MWNT has the same overall ORR activity performance as the non-doped MWNT variant, MoS_2@MWNT. An increase in the electrocatalytic performance was expected due to the presence of N-doped MWNT, which has higher reactivity.[19-21, 55]

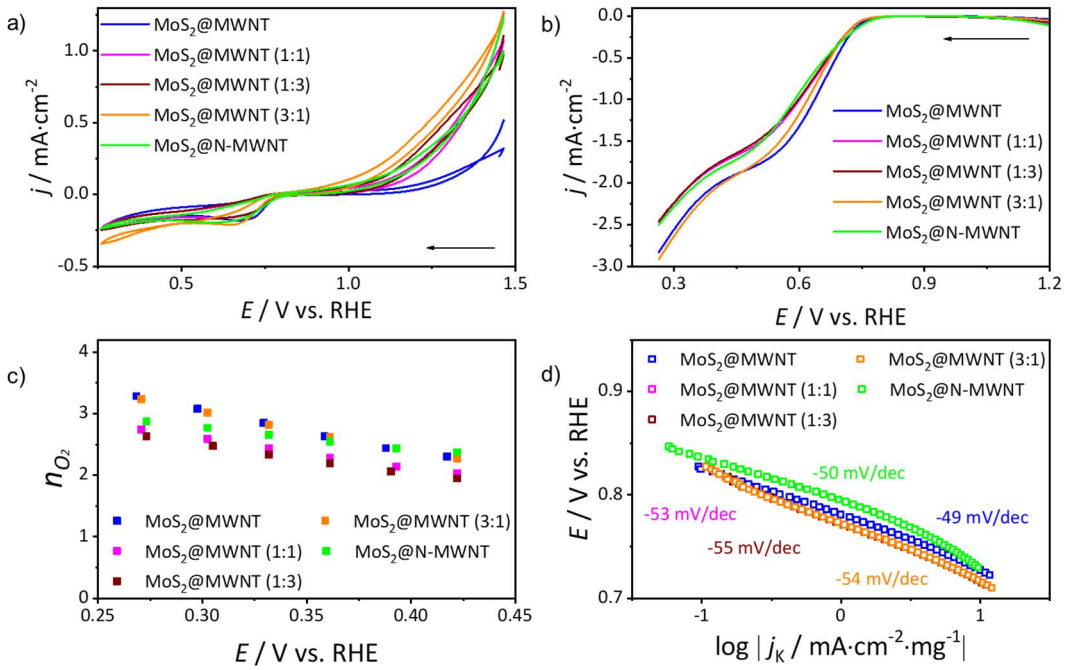

Figure 23 – Electrochemical studies on MoS_2@MWNT, MoS_2@MWNT (1:1), MoS_2@MWNT (1:3), MoS_2@MWNT (3:1), and MoS_2@N-MWNT. a) CVs (O_2-saturated 0.1 mol·dm^{-3} KOH, v = 0.005 V·s^{-1}); b) LSVs at 1600 rpm (O_2-saturated 0.1 mol·dm^{-3} KOH, v = 0.005 V·s^{-1}); c) n_{O2} at different potentials; d) Tafel plots.

3.3.2.2 OER activity performance

These materials (building blocks and nanocomposite materials) were also evaluated as potential electrocatalysts for the OER. Figure 24 presents the polarization curves obtained in an O_2-saturated 0.1 mol·dm^{-3} KOH at v = 0.005 V·s^{-1} and 1600 rpm.

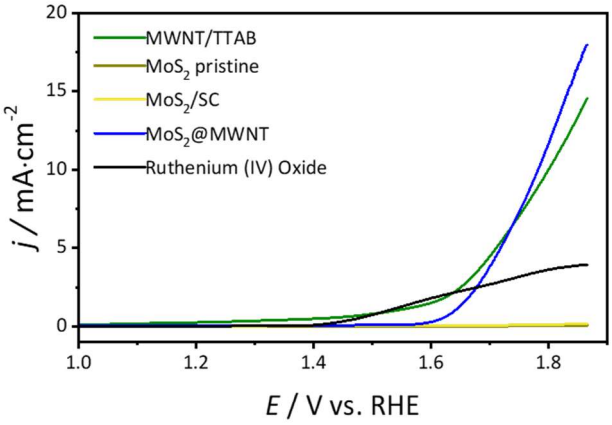

Figure 24 – OER polarization curves obtained by LSV (O_2-saturated 0.1 mol·dm^{-3} KOH, v = 0.005 V·s^{-1}, 1600 rpm) for MWNT/TTAB, MoS_2 pristine, MoS_2/SC, MoS_2@MWNT and RuO_2.

The OER activity parameters, derived from the LSV plots, are collected in Table 6. As for the WS_2 materials, both MoS_2 pristine and MoS_2/SC present the poorest OER activity, with maximum current densities of 0.071 mA·cm^{-2} for MoS_2 pristine and 0.17 mA·cm^{-2} for MoS_2/SC. Even though there is a difference between both materials (pristine and exfoliated), these do not, ultimately, show a good OER activity. Exfoliated MoS_2 particles expose the metal more easily. It was expected that MoS_2/SC had better OER activity, but the presence of surfactant may be blocking active sites.

Table 6 – OER activity parameters (η, j_{max}, and $j_{1.8}$) for MWNT/TTAB, MoS_2 pristine, MoS_2/SC, MoS_2@MWNT, and RuO_2.

Sample	**η / V** (j = 10 mA·cm^{-2})	**j_{max} / mA·cm^{-2}**	**$j_{1.8}$ / mA·cm^{-2}**
MWNT/TTAB	0.59	14.55	10.15
MoS_2 pristine	----	0.071	0.039
MoS_2/SC	----	0.17	0.12
MoS_2@MWNT	0.55	17.96	11.88
RuO_2	----	3.94	3.64

MoS_2@MWNT has the best OER activity performance of the studied materials with a j_{max} of 17.96 mA·cm^{-2} and an η of 0.55 V, outperforming the other materials evaluated.

Curiously, the nanocomposite has better OER electrocatalytic performance than the sum of its constituents, and hence synergism of properties is obtained.

As for the ORR electrocatalytic studies, variants of the MoS_2@MWNT with different MoS_2 to MWNT ratios (1:1, 1:3, and 3:1) were studied for the OER reaction, as well as a nanocomposite with N-doped MWNT. The OER LSVs of these materials are presented in Figure 25.

OER electrocatalytic performance was similar for the MoS_2@MWNT (1:1), MoS_2@MWNT (1:3), and MoS_2@MWNT (3:1) materials. Contrastingly, MoS_2@MWNT shows better OER activity performance than the variants studied. This indicates that the TMD to MWNT ratio impacts the OER performance of the materials, but only at specific values, further suggesting that a thorough investigation of the best ratio is necessary and crucial to the development of efficient electrocatalysts based on these materials.

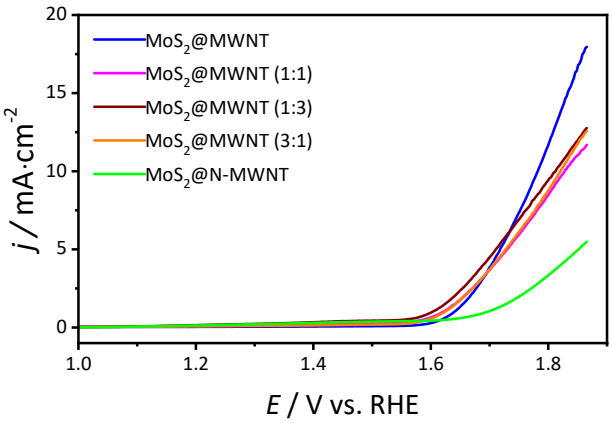

Figure 25 – OER polarization curves obtained by LSV (O_2-saturated 0.1 mol·dm^{-3} KOH, v = 0.005 V·s^{-1}, 1600 rpm) for MoS_2@MWNT, MoS_2@MWNT (1:1), MoS_2@MWNT (1:3), MoS_2@MWNT (3:1), and MoS_2@N-MWNT.

From all the materials, MoS_2@N-MWNT presented the worst performance towards OER. Again, this result was unexpected due to the high reactivity of N-doped carbon materials, as highlighted in the literature.[19-21] Possibly, the N-doped carbon wall interacts with the TMD layers, reducing the ability of these materials to adsorb O_2 and activating the reaction. Alternatively, the MoS_2 presence may be blocking OER active sites in the N-doped CNTs.

Table 7 collects the OER activity parameters studied. All materials, except MoS_2@N-MWNT, surpassed the desirable current density of j = 10 mA·cm^{-2}, with MoS_2@MWNT having the lowest overpotential value, at η = 0.55 V.

Table 7 – OER activity parameters (η, j_{max}, and $j_{1.8}$) for MoS_2@MWNT, MoS_2@MWNT (1:1), MoS_2@MWNT (1:3), MoS_2@MWNT (3:1), and MoS_2@N-MWNT

Sample	**η / V** (j = 10 mA·cm^{-2})	**j_{max} / mA·cm^{-2}**	**$j_{1.8}$ / mA·cm^{-2}**
MoS_2@MWNT	0.55	17.96	11.88
MoS_2@MWNT (1:1)	0.60	11.70	8.60
MoS_2@MWNT (1:3)	0.58	12.77	9.55
MoS_2@MWNT (3:1)	0.59	12.57	8.86
MoS_2@N-MWNT	----	5.49	3.40

3.4 Overview of the electrocatalytic performance of the nanocomposites

Considering only the nanocomposite materials assembled and tested in this work, MoS_2@MWNT has the best overall ORR and OER electrocatalytic activity. Figure 26 summarizes all the ORR studies performed with this materials, comparing CVs (a)), LSVs (b)), n_{O2} at different potentials (c)), and Tafel plots (d)).

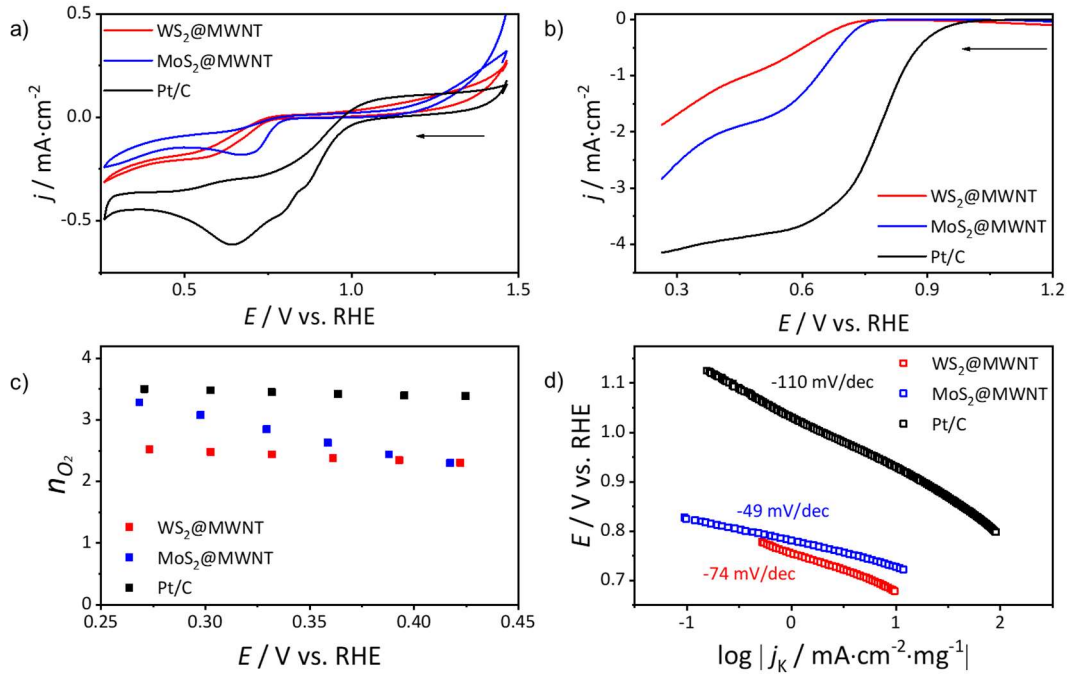

Figure 26 – Electrochemical studies on WS_2@MWNT, MoS_2@MWNT, and Pt/C. a) CVs (O_2-saturated 0.1 mol·dm^{-3} KOH, v = 0.005 V·s^{-1}); b) LSVs at 1600 rpm (O_2-saturated 0.1 mol·dm^{-3} KOH, v = 0.005 V·s^{-1}); c) n_{O2} at different potentials; d) Tafel plots.

MoS_2@MWNT outperformed WS_2@MWNT in almost every aspect studied. It has higher E_{onset} values (0.73 and 0.71 V vs. RHE, respectively), j_L values (-2.74 and -1.87, respectively) and n_{O2} values (2.87 and 2.41, respectively). However, for MoS_2@MWNT n_{O2} is more dependent on the applied potential and the Tafel slope is lower than for WS_2@MWNT. Neither material was able to outperform the Pt/C benchmark electrocatalyst.

A good electrocatalyst should also have good methanol tolerance. In methanol-based fuel cells, fuel crossover from the anode to the cathode may occur and hence reduce cathodic performance, if electrocatalysts are sensitive to methanol.[38] As such, tolerance to methanol was evaluated using chronoamperometric (CA) tests lasting 2500 s, at 1600 rpm and at E = 0.41 V vs. RHE. At the 500 s mark, 2 mL of methanol were injected in the electrolyte (0.1 mol·dm^{-3} KOH). After the CA studies, a CV was performed with methanol still in the solution, to further investigate the effect of the alcohol on the activity of the electrocatalysts. These results are collected in Figure 27.

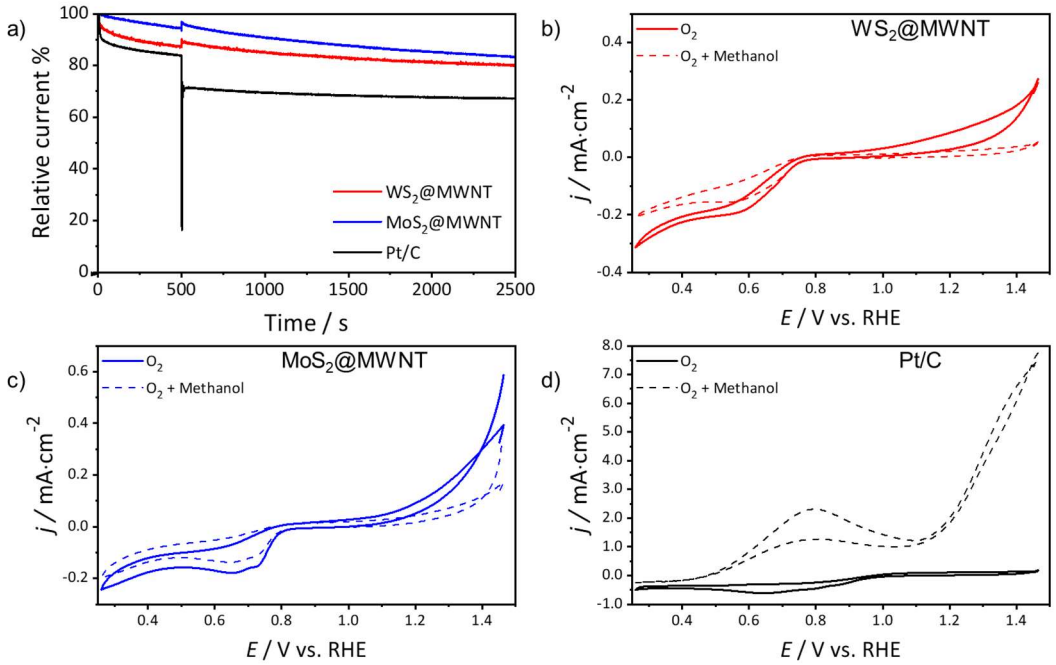

Figure 27 – Methanol resistance studies. a) chronoamperometric responses of the WS_2@MWNT, MoS_2@MWNT and Pt/C materials with the addition of 0.5 mol·dm^{-3} methanol (at 500 s); b) CV of WS_2@MWNT before and after methanol addition; c) CV of MoS_2@MWNT before and after methanol addition; d) CV of Pt/C before and after methanol addition.

As stated, platinum-based materials have the disadvantage of being highly reactive to the methanol oxidation reaction. This affects its ORR activity performance, lowering the obtained current intensity.[8, 12] This effect is visible in the CA results (Figure 27 – a)), where Pt/C underwent a decrease in ORR activity of 35%. In contrast, both nanocomposite materials showed better methanol tolerance and, subsequently, higher ORR selectivity. MoS_2@MWNT suffered a decrease in ORR activity of 18% while for WS_2@MWNT the decrease was of 20%.

Long-term stability of the electrocatalyst is another very important evaluation parameter. It was performed by CA test during 36000 s, in O_2-saturated 0.1 mol·dm^{-3} KOH, at 1600 rpm and at E = 0.41 V vs. RHE. Results are shown in Figure 28. After 36000 s, 79% of the current intensity are retained by WS_2@MWNT, while MoS_2@MWNT only retains 71%.

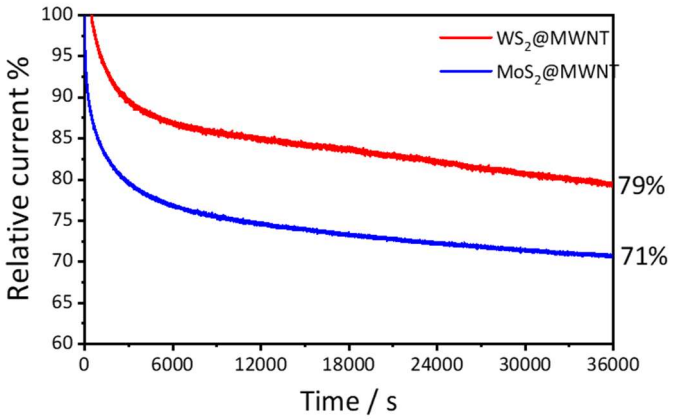

Figure 28 – Chronoamperometric response of WS_2@MWNT and MoS_2@MWNT to a potential E = 0.41 V vs. RHE (O_2-saturated 0.1 mol·dm^{-3} KOH at 1600 rpm) after 36000 s.

Concerning the electrocatalytic performance of the nanocomposite materials towards the OER, results show a large difference between them. While MoS_2@MWNT presents j_{max} values of 17.96 mA·cm^{-2} and η = 0.55 V, WS_2@MWNT only reaches current densities of j_{max} = 2.45 mA·cm^{-2}. Figure 29 summarizes the OER activity results in the LSV curves.

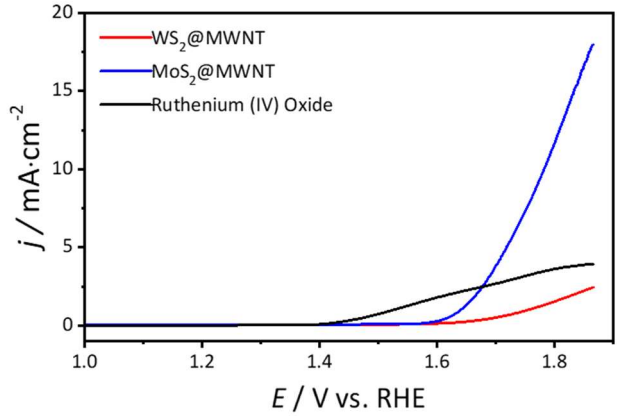

Figure 29 – OER polarization curves obtained by LSV (O_2-saturated 0.1 mol·dm^{-3} KOH, v = 0.005 V·s^{-1}, 1600 rpm) for WS_2@MWNT, MoS_2@MWNT, and RuO_2.

Overall, MoS_2@MWNT had better electrocatalytic performance than WS_2@MWNT towards the oxygen reactions. While ORR activity is modest, OER activity is good, suggesting that the nanocomposites may be developed towards bifunctional electrocatalysts, with this fabrication method.

Chapter 4

Conclusions and Future Perspectives

4 Conclusions and Future Perspectives

In this work, nanocomposites of TMDs and carbon nanomaterials were successfully assembled via a colloidal method based on surfactant-assisted dispersions and electrostatic interactions between oppositely charged surfaces. TMDs were previously functionalized with ionic surfactants and their dispersibility behavior in solution was studied. Results show that both the surfactant, the metal and the chalcogen have an impact on the final behavior and stability of the dispersions. In general, sodium cholate (SC) has higher dispersibility than cetyltrimethylammonium bromide (CTAB), while the latter shows more stability. TMDs with sulfur, S, as the chalcogen showed similar dispersibility, but WS_2 had less similar dispersibility curves than MoX TMDs, suggesting the metal has a larger effect on the overall dispersibility behavior. The obtained Raman spectra helped characterizing the dispersed TMDs as few-layers particles.

Both the TMDs dispersed in neat H_2O, SC, and CTAB and the final nanocomposite materials were characterized by SEM. The micrographs showed that neat H_2O dispersions were more aggregated, with bigger clusters, than the dispersions in aqueous surfactant solutions. The $\overline{MLD}$ of the particles was measured and TMDs dispersed in CTAB showed less polydispersity of particle size. Regarding the nanocomposites, results showed good mixture between the TMDs and MWNTs, with the carbon materials being disposed horizontally on the surface of the 2D sheets.

As proof-of-concept of the fabrication method for the nanocomposites aiming at applications, the materials were then tested as electrocatalysts. The nanocomposite materials showed electrochemical activity towards the ORR, with modest performance and good methanol tolerance. The MoS_2@MWNT nanocomposite had a value of n_{O2} close to 3 (indicating a mixed 2- and 4- electron mechanism) and a better overall ORR activity, E_{onset} and j_L values of 0.73 V vs. RHE and -2.74 mA·cm^{-2}, respectively, when compared to WS_2@MWNT (E_{onset} = 0.71 V vs. RHE; j_L = -2.07 mA·cm^{-2}). Further, MoS_2@MWNT showed good OER activity as an electrocatalyst, with η and j_{max} values of 0.55 V and 17.96 mA·cm^{-2}, respectively. These findings point towards potential improvement of the nanocomposite, in order to find the best TMD-to-MWNT ratio and develop a good bifunctional electrocatalyst, while having an easy assembly method and cost-effective production.

As suggestions for future work, further improvements could be done regarding the fine-tuning of the ratio between TMD and MWNTs. Additionally, new TMDs could be

implemented in the final nanocomposites, and tested as electrocatalysts, since different metals in the TMD have different performances, as seen in this work.

The impact of the chalcogen in the TMD can also be studied. It is widely accepted that the edges of layered nanomaterials are more active than the basal plane.[18, 62] In TMDs, the edges of the particles are comprised of chalcogen atoms. As such, different chalcogens in the TMD should impact the electrochemical performance of the final nanocomposite.

The incorporation of other carbon nanomaterials, such as graphene or carbon nanofibers and nanorods, could also be studied. The assembly method allows the building of nanocomposites with more than two constituents, and so other carbon allotropes can be added to the final material or substitute the MWNTs. These carbon materials may also be doped, since results in literature tend to highlight the advantage of doped materials.[19-21]

References

1. Volta, A., On the electricity excited by the mere contact of conducting substances of different kinds. *Philosophical Transactions of The Royal Society of London* **1800,** *90*.

2. Shafiee, S.; Topal, E., When will fossil fuel reserves be diminished? *Energy Policy* **2009,** *37*, 181-189.

3. Robyns, B.; Davigny, A.; François, B.; Henneton, A.; Sprooten, J., *Electricity Production from Renewable Energies*. 1st ed.; Wiley: Hoboken, NJ, 2012.

4. Aneke, M.; Wang, M., Energy storage technologies and real life applications – A state of the art review. *Applied Energy* **2016,** *179*, 350-377.

5. Seh, Z. W.; Kibsgaard, J.; Dickens, C. F.; Chorkendorff, I.; Nørskov, J. K.; Jaramillo, T. F., Combining theory and experiment in electrocatalysis: Insights into materials design. *Science* **2017,** *355*, eaad4998.

6. Kuang, M.; Zheng, G., Nanostructured Bifunctional Redox Electrocatalysts. *Small* **2016,** *12*, 5656-5675.

7. Breeze, P., Chapter 1 - An Introduction to Fuel Cells. In *Fuel Cells*, Breeze, P., Ed. Academic Press: 2017; pp 1-10.

8. Freire, C.; Fernandes, D. M.; Nunes, M.; Abdelkader, V. K., POM & MOF-based Electrocatalysts for Energy-related Reactions. *ChemCatChem* **2018,** *10*, 1703-1730.

9. Kaur, M.; Pal, K., Review on hydrogen storage materials and methods from an electrochemical viewpoint. *Journal of Energy Storage* **2019,** *23*, 234-249.

10. Zhu, Y. P.; Guo, C.; Zheng, Y.; Qiao, S.-Z., Surface and Interface Engineering of Noble-Metal-Free Electrocatalysts for Efficient Energy Conversion Processes. *Accounts of Chemical Research* **2017,** *50*, 915-923.

11. Anantharaj, S.; Ede, S. R.; Sakthikumar, K.; Karthick, K.; Mishra, S.; Kundu, S., Recent Trends and Perspectives in Electrochemical Water Splitting with an

Emphasis on Sulfide, Selenide, and Phosphide Catalysts of Fe, Co, and Ni: A Review. *ACS Catalysis* **2016,** *6*, 8069-8097.

12. Fernandes, D. M.; Novais, H. C.; Bacsa, R.; Serp, P.; Bachiller-Baeza, B.; Rodríguez-Ramos, I.; Guerrero-Ruiz, A.; Freire, C., Polyoxotungstate@Carbon Nanocomposites As Oxygen Reduction Reaction (ORR) Electrocatalysts. *Langmuir* **2018,** *34*, 6376-6387.

13. Shi, H.; Shen, Y.; He, F.; Li, Y.; Liu, A.; Liu, S.; Zhang, Y., Recent advances of doped carbon as non-precious catalysts for oxygen reduction reaction. *Journal of Materials Chemistry A* **2014,** *2*, 15704-15716.

14. Jiao, Y.; Zheng, Y.; Jaroniec, M.; Qiao, S. Z., Design of electrocatalysts for oxygen- and hydrogen-involving energy conversion reactions. *Chemical Society Reviews* **2015,** *44*, 2060-2086.

15. Katsounaros, I.; Cherevko, S.; Zeradjanin, A. R.; Mayrhofer, K. J. J., Oxygen Electrochemistry as a Cornerstone for Sustainable Energy Conversion. *Angewandte Chemie International Edition* **2014,** *53*, 102-121.

16. Bard, A. J.; Faulkner, L. R., *Electrochemical Methods: Fundamentals and Applications*. 2nd ed.; Wiley: New York, 2001.

17. Daems, N.; Sheng, X.; Vankelecom, I. F. J.; Pescarmona, P. P., Metal-free doped carbon materials as electrocatalysts for the oxygen reduction reaction. *Journal of Materials Chemistry A* **2014,** *2*, 4085-4110.

18. Shen, A.; Zou, Y.; Wang, Q.; Dryfe, R. A. W.; Huang, X.; Dou, S.; Dai, L.; Wang, S., Oxygen Reduction Reaction in a Droplet on Graphite: Direct Evidence that the Edge Is More Active than the Basal Plane. *Angewandte Chemie International Edition* **2014,** *53*, 10804-10808.

19. Tuci, G.; Zafferoni, C.; Rossin, A.; Milella, A.; Luconi, L.; Innocenti, M.; Truong Phuoc, L.; Duong-Viet, C.; Pham-Huu, C.; Giambastiani, G., Chemically Functionalized Carbon Nanotubes with Pyridine Groups as Easily Tunable N-Decorated Nanomaterials for the Oxygen Reduction Reaction in Alkaline Medium. *Chemistry of Materials* **2014,** *26*, 3460-3470.

20. Vikkisk, M.; Kruusenberg, I.; Ratso, S.; Joost, U.; Shulga, E.; Kink, I.; Rauwel, P.; Tammeveski, K., Enhanced electrocatalytic activity of nitrogen-doped multi-

walled carbon nanotubes towards the oxygen reduction reaction in alkaline media. *RSC Advances* **2015,** *5*, 59495-59505.

21. Wu, J.; Ma, L.; Yadav, R. M.; Yang, Y.; Zhang, X.; Vajtai, R.; Lou, J.; Ajayan, P. M., Nitrogen-Doped Graphene with Pyridinic Dominance as a Highly Active and Stable Electrocatalyst for Oxygen Reduction. *ACS Applied Materials & Interfaces* **2015,** *7*, 14763-14769.

22. Niu, W.-J.; Zhu, R.-H.; Yan, H.; Zeng, H.-B.; Cosnier, S.; Zhang, X.-J.; Shan, D., One-pot synthesis of nitrogen-rich carbon dots decorated graphene oxide as metal-free electrocatalyst for oxygen reduction reaction. *Carbon* **2016,** *109*, 402-410.

23. Zhou, L.; Fu, P.; Wang, Y.; Sun, L.; Yuan, Y., Microbe-engaged synthesis of carbon dot-decorated reduced graphene oxide as high-performance oxygen reduction catalysts. *Journal of Materials Chemistry A* **2016,** *4*, 7222-7229.

24. Fan, T.; Zhang, G.; Jian, L.; Murtaza, I.; Meng, H.; Liu, Y.; Min, Y., Facile synthesis of defect-rich nitrogen and sulfur Co-doped graphene quantum dots as metal-free electrocatalyst for the oxygen reduction reaction. *Journal of Alloys and Compounds* **2019,** *792*, 844-850.

25. Faraji, M.; Derakhshi, P.; Tahvildari, K.; Yousefian, Z., High performance Fe and N-codoped graphene quantum dot supported Pd3Co catalyst with synergistically improved oxygen reduction activity and great methanol tolerance. *Solid State Sciences* **2018,** *83*, 152-160.

26. Liu, K.; Song, Y.; Chen, S., Oxygen reduction catalyzed by nanocomposites based on graphene quantum dots-supported copper nanoparticles. *International Journal of Hydrogen Energy* **2016,** *41*, 1559-1567.

27. Tian, G.-L.; Zhao, M.-Q.; Yu, D.; Kong, X.-Y.; Huang, J.-Q.; Zhang, Q.; Wei, F., Nitrogen-Doped Graphene/Carbon Nanotube Hybrids: In Situ Formation on Bifunctional Catalysts and Their Superior Electrocatalytic Activity for Oxygen Evolution/Reduction Reaction. *Small* **2014,** *10*, 2251-2259.

28. Suntivich, J.; May, K. J.; Gasteiger, H. A.; Goodenough, J. B.; Shao-Horn, Y., A Perovskite Oxide Optimized for Oxygen Evolution Catalysis from Molecular Orbital Principles. *Science* **2011,** *334*, 1383.

29. Wurster, B.; Grumelli, D.; Hötger, D.; Gutzler, R.; Kern, K., Driving the Oxygen Evolution Reaction by Nonlinear Cooperativity in Bimetallic Coordination Catalysts. *Journal of the American Chemical Society* **2016,** *138*, 3623-3626.

30. Li, M.; Xiong, Y.; Liu, X.; Bo, X.; Zhang, Y.; Han, C.; Guo, L., Facile synthesis of electrospun MFe2O4 (M = Co, Ni, Cu, Mn) spinel nanofibers with excellent electrocatalytic properties for oxygen evolution and hydrogen peroxide reduction. *Nanoscale* **2015,** *7*, 8920-8930.

31. Voiry, D.; Salehi, M.; Silva, R.; Fujita, T.; Chen, M.; Asefa, T.; Shenoy, V. B.; Eda, G.; Chhowalla, M., Conducting MoS2 Nanosheets as Catalysts for Hydrogen Evolution Reaction. *Nano Letters* **2013,** *13*, 6222-6227.

32. Cheng, Y.; Song, H.; Wu, H.; Zhang, P.; Tang, Z.; Lu, S., Defects Enhance the Electrocatalytic Hydrogen Evolution Properties of MoS2-based Materials. *Chemistry – An Asian Journal* **2020,** *n/a*.

33. de-Mello, G. B.; Smith, L.; Rowley-Neale, S. J.; Gruber, J.; Hutton, S. J.; Banks, C. E., Surfactant-exfoliated 2D molybdenum disulphide (2D-MoS2): the role of surfactant upon the hydrogen evolution reaction. *RSC Advances* **2017,** *7*, 36208-36213.

34. Georgakilas, V.; Perman, J. A.; Tucek, J.; Zboril, R., Broad Family of Carbon Nanoallotropes: Classification, Chemistry, and Applications of Fullerenes, Carbon Dots, Nanotubes, Graphene, Nanodiamonds, and Combined Superstructures. *Chemical Reviews* **2015,** *115*, 4744-4822.

35. Kroto, H. W.; Heath, J. R.; O'Brien, S. C.; Curl, R. F.; Smalley, R. E., C60: Buckminsterfullerene. *Nature* **1985,** *318*, 162-163.

36. Iijima, S., Helical microtubules of graphitic carbon. *Nature* **1991,** *354*, 56-58.

37. Wang, D.-W.; Su, D., Heterogeneous nanocarbon materials for oxygen reduction reaction. *Energy & Environmental Science* **2014,** *7*, 576-591.

38. Zhang, B.-T.; Zheng, X.; Li, H.-F.; Lin, J.-M., Application of carbon-based nanomaterials in sample preparation: A review. *Analytica Chimica Acta* **2013,** *784*, 1-17.

39. Liu, Q.; Shi, J.; Zeng, L.; Wang, T.; Cai, Y.; Jiang, G., Evaluation of graphene as an advantageous adsorbent for solid-phase extraction with chlorophenols as model analytes. *Journal of Chromatography A* **2011,** *1218*, 197-204.

40. Bae, S.; Kim, H.; Lee, Y.; Xu, X.; Park, J.-S.; Zheng, Y.; Balakrishnan, J.; Lei, T.; Ri Kim, H.; Song, Y. I.; Kim, Y.-J.; Kim, K. S.; Özyilmaz, B.; Ahn, J.-H.; Hong, B. H.; Iijima, S., Roll-to-roll production of 30-inch graphene films for transparent electrodes. *Nature Nanotechnology* **2010,** *5*, 574-578.

41. Juang, Z.-Y.; Wu, C.-Y.; Lu, A.-Y.; Su, C.-Y.; Leou, K.-C.; Chen, F.-R.; Tsai, C.-H., Graphene synthesis by chemical vapor deposition and transfer by a roll-to-roll process. *Carbon* **2010,** *48*, 3169-3174.

42. Polsen, E. S.; McNerny, D. Q.; Viswanath, B.; Pattinson, S. W.; John Hart, A., High-speed roll-to-roll manufacturing of graphene using a concentric tube CVD reactor. *Scientific Reports* **2015,** *5*, 10257.

43. Zhang, J.; Terrones, M.; Park, C. R.; Mukherjee, R.; Monthioux, M.; Koratkar, N.; Kim, Y. S.; Hurt, R.; Frackowiak, E.; Enoki, T.; Chen, Y.; Chen, Y.; Bianco, A., Carbon science in 2016: Status, challenges and perspectives. *Carbon* **2016,** *98*, 708-732.

44. Reina, G.; González-Domínguez, J. M.; Criado, A.; Vázquez, E.; Bianco, A.; Prato, M., Promises, facts and challenges for graphene in biomedical applications. *Chemical Society Reviews* **2017,** *46*, 4400-4416.

45. Trogadas, P.; Fuller, T. F.; Strasser, P., Carbon as catalyst and support for electrochemical energy conversion. *Carbon* **2014,** *75*, 5-42.

46. Hussain, C. M.; Mitra, S., Micropreconcentration units based on carbon nanotubes (CNT). *Analytical and Bioanalytical Chemistry* **2011,** *399*, 75-89.

47. Peigney, A.; Laurent, C.; Flahaut, E.; Bacsa, R.; Rousset, A., Specific Surface Area of Carbon Nanotubes and Bundles of Carbon Nanotubes. *Carbon* **2001,** *39*, 507-514.

48. Terrones, M., Science and Technology of the Twenty-First Century: Synthesis, Properties, and Applications of Carbon Nanotubes. *Annual Review of Materials Research* **2003,** *33*, 419-501.

49. Kumar, M.; Ando, Y., Chemical Vapor Deposition of Carbon Nanotubes: A Review on Growth Mechanism and Mass Production. *Journal of Nanoscience and Nanotechnology* **2010,** *10*, 3739-3758.

50. Eder, D., Carbon Nanotube−Inorganic Hybrids. *Chemical Reviews* **2010,** *110*, 1348-1385.

51. Vidu, R.; Rahman, M.; Mahmoudi, M.; Enachescu, M.; Poteca, T. D.; Opris, I., Nanostructures: a platform for brain repair and augmentation. *Frontiers in Systems Neuroscience* **2014,** *8*.

52. Panchakarla, L. S.; Govindaraj, A.; Rao, C. N. R., Boron- and nitrogen-doped carbon nanotubes and graphene. *Inorganica Chimica Acta* **2010,** *363*, 4163-4174.

53. Wang, H.; Maiyalagan, T.; Wang, X., Review on Recent Progress in Nitrogen-Doped Graphene: Synthesis, Characterization, and Its Potential Applications. *ACS Catalysis* **2012,** *2*, 781-794.

54. Terrones, M.; Filho, A. G. S.; Rao, A. M., Doped Carbon Nanotubes: Synthesis, Characterization and Applications. In *Carbon Nanotubes: Advanced Topics in the Synthesis, Structure, Properties and Applications*, Jorio, A.; Dresselhaus, G.; Dresselhaus, M. S., Eds. Springer Berlin Heidelberg: Berlin, Heidelberg, 2008; pp 531-566.

55. Ayala, P.; Arenal, R.; Rümmeli, M.; Rubio, A.; Pichler, T., The doping of carbon nanotubes with nitrogen and their potential applications. *Carbon* **2010,** *48*, 575-586.

56. Soares, O. S. G. P.; Rocha, R. P.; Órfão, J. J. M.; Pereira, M. F. R.; Figueiredo, J. L., Mechanothermal Approach for N-, S-, P-, and B-Doping of Carbon Nanotubes: Methodology and Catalytic Performance in Wet Air Oxidation. *C* **2019,** *5*, 30.

57. Tang, Q.; Zhou, Z., Graphene-analogous low-dimensional materials. *Progress in Materials Science* **2013,** *58*, 1244-1315.

58. Mas-Ballesté, R.; Gómez-Navarro, C.; Gómez-Herrero, J.; Zamora, F., 2D materials: to graphene and beyond. *Nanoscale* **2011,** *3*, 20-30.

59. Novoselov, K. S.; Jiang, D.; Schedin, F.; Booth, T. J.; Khotkevich, V. V.; Morozov, S. V.; Geim, A. K., Two-dimensional atomic crystals. *Proceedings of the National Academy of Sciences of the United States of America* **2005,** *102*, 10451.

60. Miró, P.; Audiffred, M.; Heine, T., An atlas of two-dimensional materials. *Chemical Society Reviews* **2014,** *43*, 6537-6554.

61. Rapoport, L.; Moshkovich, A.; Perfilyev, V.; Lapsker, I.; Halperin, G.; Itovich, Y.; Etsion, I., Friction and wear of MoS2 films on laser textured steel surfaces. *Surface and Coatings Technology* **2008,** *202*, 3332-3340.

62. Gupta, D.; Chauhan, V.; Kumar, R., A comprehensive review on synthesis and applications of molybdenum disulfide (MoS2) material: Past and recent developments. *Inorganic Chemistry Communications* **2020,** *121*, 108200.

63. Xu, M.; Liang, T.; Shi, M.; Chen, H., Graphene-Like Two-Dimensional Materials. *Chemical Reviews* **2013,** *113*, 3766-3798.

64. McCreery, R. L., Advanced Carbon Electrode Materials for Molecular Electrochemistry. *Chemical Reviews* **2008,** *108*, 2646-2687.

65. Drisko, G. L.; Sanchez, C., Hybridization in Materials Science – Evolution, Current State, and Future Aspirations. *European Journal of Inorganic Chemistry* **2012,** *2012*, 5097-5105.

66. Alemán, J. V.; Chadwick, A. V.; He, J.; Hess, M.; Horie, K.; Jones, R. G.; Kratochvíl, P.; Meisel, I.; Mita, I.; Moad, G.; Penczek, S.; Stepto, R. F. T., Definitions of terms relating to the structure and processing of sols, gels, networks, and inorganic-organic hybrid materials (IUPAC Recommendations 2007). *Pure and Applied Chemistry* **2007,** *79*, 1801-1829.

67. Le, B.; Khaliq, J.; Huo, D.; Teng, X.; Shyha, I., A Review on Nanocomposites. Part 1: Mechanical Properties. *Journal of Manufacturing Science and Engineering* **2020,** *142*.

68. Christopher Igwe, I.; Azman, H., Emerging trends in graphene carbon based polymer nanocomposites and applications. *Reviews in Chemical Engineering* **2016,** *32*, 223-264.

69. Rahaman, M.; Chaki, T. K.; Khastgir, D., Development of high performance EMI shielding material from EVA, NBR, and their blends: effect of carbon black structure. *Journal of Materials Science* **2011,** *46*, 3989-3999.

70. Wang, L.; Ye, Y.; Lu, X.; Wen, Z.; Li, Z.; Hou, H.; Song, Y., Hierarchical Nanocomposites of Polyaniline Nanowire Arrays on Reduced Graphene Oxide Sheets for Supercapacitors. *Scientific Reports* **2013,** *3*, 3568.

71. Zhou, Y.; Jiang, Y.; Xie, G.; Wu, M.; Tai, H., Gas sensors for CO2 detection based on RGO–PEI films at room temperature. *Chinese Science Bulletin* **2014,** *59*, 1999-2005.

72. Wang, L.; Ye, Y.; Shen, Y.; Wang, F.; Lu, X.; Xie, Y.; Chen, S.; Tan, H.; Xu, F.; Song, Y., Hierarchical nanocomposites of Co3O4/polyaniline nanowire arrays/reduced graphene oxide sheets for amino acid detection. *Sensors and Actuators B: Chemical* **2014,** *203*, 864-872.

73. Shi, C.; Owusu, K. A.; Xu, X.; Zhu, T.; Zhang, G.; Yang, W.; Mai, L., 1D Carbon-Based Nanocomposites for Electrochemical Energy Storage. *Small* **2019,** *15*, 1902348.

74. Xia, X.; Chao, D.; Zhang, Y.; Zhan, J.; Zhong, Y.; Wang, X.; Wang, Y.; Shen, Z. X.; Tu, J.; Fan, H. J., Generic Synthesis of Carbon Nanotube Branches on Metal Oxide Arrays Exhibiting Stable High-Rate and Long-Cycle Sodium-Ion Storage. *Small* **2016,** *12*, 3048-3058.

75. Yin, H.; Qu, H.-Q.; Liu, Z.; Jiang, R.-Z.; Li, C.; Zhu, M.-Q., Long cycle life and high rate capability of three dimensional CoSe2 grain-attached carbon nanofibers for flexible sodium-ion batteries. *Nano Energy* **2019,** *58*, 715-723.

76. Yang, H.; Wang, M.; Liu, X.; Jiang, Y.; Yu, Y., MoS2 embedded in 3D interconnected carbon nanofiber film as a free-standing anode for sodium-ion batteries. *Nano Research* **2018,** *11*, 3844-3853.

77. Kim, Y.; Park, T.; Na, J.; Yi, J. W.; Kim, J.; Kim, M.; Bando, Y.; Yamauchi, Y.; Lin, J., Layered transition metal dichalcogenide/carbon nanocomposites for electrochemical energy storage and conversion applications. *Nanoscale* **2020,** *12*, 8608-8625.

78. Xu, S.; Lei, Z.; Wu, P., Facile preparation of 3D MoS2/MoSe2 nanosheet–graphene networks as efficient electrocatalysts for the hydrogen evolution reaction. *Journal of Materials Chemistry A* **2015,** *3*, 16337-16347.

79. Tan, C.; Luo, Z.; Chaturvedi, A.; Cai, Y.; Du, Y.; Gong, Y.; Huang, Y.; Lai, Z.; Zhang, X.; Zheng, L.; Qi, X.; Goh, M. H.; Wang, J.; Han, S.; Wu, X.-J.; Gu, L.; Kloc, C.; Zhang, H., Preparation of High-Percentage 1T-Phase Transition Metal Dichalcogenide Nanodots for Electrochemical Hydrogen Evolution. *Advanced Materials* **2018,** *30*, 1705509.

80. Cao, J.; Zhou, J.; Zhang, Y.; Liu, X., A Clean and Facile Synthesis Strategy of MoS2 Nanosheets Grown on Multi-Wall CNTs for Enhanced Hydrogen Evolution Reaction Performance. *Scientific Reports* **2017,** *7*, 8825.

81. Zhang, S.; Yu, X.; Yu, H.; Chen, Y.; Gao, P.; Li, C.; Zhu, C., Growth of Ultrathin MoS2 Nanosheets with Expanded Spacing of (002) Plane on Carbon Nanotubes for High-Performance Sodium-Ion Battery Anodes. *ACS Applied Materials & Interfaces* **2014,** *6*, 21880-21885.

82. Lau, Y. J.; Khan, F. S. A.; Mubarak, N. M.; Lau, S. Y.; Chua, H. B.; Khalid, M.; Abdullah, E. C., Chapter 10 - Functionalized carbon nanomaterials for wastewater treatment. In *Industrial Applications of Nanomaterials*, Thomas, S.; Grohens, Y.; Pottathara, Y. B., Eds. Elsevier: 2019; pp 283-311.

83. Karousis, N.; Tagmatarchis, N.; Tasis, D., Current Progress on the Chemical Modification of Carbon Nanotubes. *Chemical Reviews* **2010,** *110*, 5366-5397.

84. Kuila, T.; Bose, S.; Mishra, A. K.; Khanra, P.; Kim, N. H.; Lee, J. H., Chemical functionalization of graphene and its applications. *Progress in Materials Science* **2012,** *57*, 1061-1105.

85. Mason, T. J., *Sonochemistry*. 1st ed.; Oxford University Press: New York, 1999.

86. Marques, E. F.; Silva, B. F. B., Surfactants, Phase Behavior. In *Encyclopedia of Colloid and Interface Science*, Tadros, T., Ed. Springer Berlin Heidelberg: Berlin, Heidelberg, 2013; pp 1290-1333.

87. Holmberg, K.; Jönsson, B.; Kronberg, B.; Lindman, B., *Surfactants and Polymers in Aqueous Solution*. 2nd ed.; John Wiley & Sons: West Sussex, UK, 2003.

88. Chang, H.; Wang, G.; Yang, A.; Tao, X.; Liu, X.; Shen, Y.; Zheng, Z., A Transparent, Flexible, Low-Temperature, and Solution-Processible Graphene Composite Electrode. *Advanced Functional Materials* **2010,** *20*, 2893-2902.

89. Zeng, Q.; Cheng, J.; Tang, L.; Liu, X.; Liu, Y.; Li, J.; Jiang, J., Self-Assembled Graphene–Enzyme Hierarchical Nanostructures for Electrochemical Biosensing. *Advanced Functional Materials* **2010,** *20*, 3366-3372.

90. Abreu, B.; Rocha, J.; Fernandes, R. M. F.; Regev, O.; Furó, I.; Marques, E. F., Gemini surfactants as efficient dispersants of multiwalled carbon nanotubes: Interplay of molecular parameters on nanotube dispersibility and debundling. *Journal of Colloid and Interface Science* **2019,** *547*, 69-77.

91. Dai, J.; Fernandes, R. M. F.; Regev, O.; Marques, E. F.; Furó, I., Dispersing Carbon Nanotubes in Water with Amphiphiles: Dispersant Adsorption, Kinetics, and Bundle Size Distribution as Defining Factors. *The Journal of Physical Chemistry C* **2018,** *122*, 24386-24393.

92. Fernandes, R. M. F.; Abreu, B.; Claro, B.; Buzaglo, M.; Regev, O.; Furó, I.; Marques, E. F., Dispersing Carbon Nanotubes with Ionic Surfactants under Controlled Conditions: Comparisons and Insight. *Langmuir* **2015,** *31*, 10955-10965.

93. Jarrais, B.; Guedes, A.; Freire, C., Heteroatom-Doped Carbon Nanomaterials as Metal-Free Catalysts for the Reduction of 4-Nitrophenol. *ChemistrySelect* **2018,** *3*, 1737-1748.

94. Smith, R. J.; King, P. J.; Lotya, M.; Wirtz, C.; Khan, U.; De, S.; O'Neill, A.; Duesberg, G. S.; Grunlan, J. C.; Moriarty, G.; Chen, J.; Wang, J.; Minett, A. I.; Nicolosi, V.; Coleman, J. N., Large-Scale Exfoliation of Inorganic Layered Compounds in Aqueous Surfactant Solutions. *Advanced Materials* **2011,** *23*, 3944-3948.

95. Coleman, J. N.; Lotya, M.; O'Neill, A.; Bergin, S. D.; King, P. J.; Khan, U.; Young, K.; Gaucher, A.; De, S.; Smith, R. J.; Shvets, I. V.; Arora, S. K.; Stanton, G.; Kim, H.-Y.; Lee, K.; Kim, G. T.; Duesberg, G. S.; Hallam, T.; Boland, J. J.; Wang, J. J.; Donegan, J. F.; Grunlan, J. C.; Moriarty, G.; Shmeliov, A.; Nicholls, R. J.; Perkins, J. M.; Grieveson, E. M.; Theuwissen, K.; McComb, D. W.; Nellist, P. D.; Nicolosi, V., Two-Dimensional Nanosheets Produced by Liquid Exfoliation of Layered Materials. *Science* **2011,** *331*, 568.

96. Skoog, D. A.; Holler, F. J.; Crouch, S. R., *Principles of Instrumental Analysis*. 6th ed.; Thomson Brooks/Cole: Belmont, CA, 2006.

97. Ohshima, H., Zeta Potential. In *Encyclopedia of Colloid and Interface Science*, Tadros, T., Ed. Springer Berlin Heidelberg: Berlin, Heidelberg, 2013; pp 1423-1436.

98. Hunter, R. J., *Zeta Potential in Colloid Science: Principles and Applications*. 1st ed.; Academic Press: London, 1981.

99. Sun, Z.; Nicolosi, V.; Rickard, D.; Bergin, S. D.; Aherne, D.; Coleman, J. N., Quantitative Evaluation of Surfactant-stabilized Single-walled Carbon Nanotubes: Dispersion Quality and Its Correlation with Zeta Potential. *The Journal of Physical Chemistry C* **2008,** *112*, 10692-10699.

100. Leng, Y., *Materials Characterization - Introduction to Microscopic and Spectroscopic Methods*. 1st ed.; Wiley: Singapore, 2008.

101. McCreery, R. L., *Raman Spectroscopy for Chemical Analysis*. 1st ed.; Wiley-Interscience: New York, 2000.

102. Zhou, X.; Qiao, J.; Yang, L.; Zhang, J., A Review of Graphene-Based Nanostructural Materials for Both Catalyst Supports and Metal-Free Catalysts in PEM Fuel Cell Oxygen Reduction Reactions. *Advanced Energy Materials* **2014,** *4*, 1301523.

103. Asakura, S.; Oosawa, F., On Interaction between Two Bodies Immersed in a Solution of Macromolecules. *The Journal of Chemical Physics* **1954,** *22*, 1255-1256.

104. Gupta, A.; Arunachalam, V.; Vasudevan, S., Water Dispersible, Positively and Negatively Charged MoS2 Nanosheets: Surface Chemistry and the Role of Surfactant Binding. *The Journal of Physical Chemistry Letters* **2015,** *6*, 739-744.

105. Gupta, A.; Vasudevan, S., Understanding Surfactant Stabilization of MoS2 Nanosheets in Aqueous Dispersions from Zeta Potential Measurements and Molecular Dynamics Simulations. *The Journal of Physical Chemistry C* **2018,** *122*, 19243-19250.

106. Lee, C.; Yan, H.; Brus, L. E.; Heinz, T. F.; Hone, J.; Ryu, S., Anomalous Lattice Vibrations of Single- and Few-Layer MoS2. *ACS Nano* **2010,** *4*, 2695-2700.

107. Li, H.; Zhang, Q.; Yap, C. C. R.; Tay, B. K.; Edwin, T. H. T.; Olivier, A.; Baillargeat, D., From Bulk to Monolayer MoS2: Evolution of Raman Scattering. *Advanced Functional Materials* **2012,** *22*, 1385-1390.

108. Saito, R.; Tatsumi, Y.; Huang, S.; Ling, X.; Dresselhaus, M. S., Raman spectroscopy of transition metal dichalcogenides. *Journal of Physics: Condensed Matter* **2016,** *28*, 353002.

109. Zhang, X.; Qiao, X.-F.; Shi, W.; Wu, J.-B.; Jiang, D.-S.; Tan, P.-H., Phonon and Raman scattering of two-dimensional transition metal dichalcogenides from monolayer, multilayer to bulk material. *Chemical Society Reviews* **2015,** *44*, 2757-2785.

110. Wang, F.; Kinloch, I. A.; Wolverson, D.; Tenne, R.; Zak, A.; O'Connell, E.; Bangert, U.; Young, R. J., Strain-induced phonon shifts in tungsten disulfide nanoplatelets and nanotubes. *2D Materials* **2016,** *4*, 015007.

111. Tonndorf, P.; Schmidt, R.; Böttger, P.; Zhang, X.; Börner, J.; Liebig, A.; Albrecht, M.; Kloc, C.; Gordan, O.; Zahn, D. R. T.; Michaelis de Vasconcellos, S.; Bratschitsch, R., Photoluminescence emission and Raman response of monolayer MoS2, MoSe2, and WSe2. *Opt. Express* **2013,** *21*, 4908-4916.

112. Liang, L.; Meunier, V., First-principles Raman spectra of MoS2, WS2 and their heterostructures. *Nanoscale* **2014,** *6*, 5394-5401.

113. Fernandes, D. M.; Mathumba, P.; Fernandes, A. J. S.; Iwuoha, E. I.; Freire, C., Towards efficient oxygen reduction reaction electrocatalysts through graphene doping. *Electrochimica Acta* **2019,** *319*, 72-81.